Redox Biology 71 (2024) 103091

Contents lists available at ScienceDirect

Redox Biology

journal homepage: www.elsevier.com/locate/redox

SOD2 orchestrates redox homeostasis in intervertebral discs: A novel insight into oxidative stress-mediated degeneration and therapeutic potential

Shota Tamagawa [a,b], Daisuke Sakai [a,*], Hidetoshi Nojiri [b], Yoshihiko Nakamura [a], Takayuki Warita [a], Erika Matsushita [a], Jordy Schol [a], Hazuki Soma [a], Shota Ogasawara [a], Daiki Munesada [a], Masato Koike [b], Takahiko Shimizu [c], Masato Sato [a], Muneaki Ishijima [b], Masahiko Watanabe [a]

[a] Department of Orthopaedic Surgery, Surgical Science, Tokai University School of Medicine, Isehara, Japan
[b] Department of Medicine for Orthopaedics and Motor Organ, Juntendo University Graduate School of Medicine, Tokyo, Japan
[c] Aging Stress Response Research Project Team, National Center for Geriatrics and Gerontology, Obu, Japan

ARTICLE INFO

Keywords:
Low back pain
Intervertebral disc degeneration
Oxidative stress
Superoxide dismutase 2
Aging
Mechanical stress

ABSTRACT

Low back pain (LBP) is a pervasive global health concern, primarily associated with intervertebral disc (IVD) degeneration. Although oxidative stress has been shown to contribute to IVD degeneration, the underlying mechanisms remain undetermined. This study aimed to unravel the role of superoxide dismutase 2 (SOD2) in IVD pathogenesis and target oxidative stress to limit IVD degeneration. SOD2 demonstrated a dynamic regulation in surgically excised human IVD tissues, with initial upregulation in moderate degeneration and downregulation in severely degenerated IVDs. Through a comprehensive set of in vitro and in vivo experiments, we found a suggestive association between excessive mitochondrial superoxide, cellular senescence, and matrix degradation in human and mouse IVD cells. We confirmed that aging and mechanical stress, established triggers for IVD degeneration, escalated mitochondrial superoxide levels in mouse models. Critically, chondrocyte-specific *Sod2* deficiency accelerated age-related and mechanical stress-induced disc degeneration in mice, and could be attenuated by β-nicotinamide mononucleotide treatment. These revelations underscore the central role of SOD2 in IVD redox balance and unveil potential therapeutic avenues, making SOD2 and mitochondrial superoxide promising targets for effective LBP interventions.

1. Introduction

Low back pain (LBP) is a pervasive global health issue that affects individuals across various age groups, leading to substantial socioeconomic burdens [1–3]. Although the causes of LBP are multifactorial [4], intervertebral disc (IVD) degeneration stands out as a primary etiological factor [5,6]. Unlike other musculoskeletal structures, IVD degeneration can initiate early in adolescence [7], making it a significant precursor for various spinal disorders, including disc herniation, spinal canal stenosis, and spinal deformities [8]. The currently available treatments are primarily palliative (e.g., analgesics or physical therapy) or involve invasive surgeries, in which both types fail to target the underlying pathology, underlining an urgent need for disease-modifying therapies [9,10]. This inadequacy is not only a cause for concern but also a reflection of our incomplete understanding of the discs' pathological mechanisms.

The IVD, critical for spinal flexibility and load distribution, comprises three distinct compartments: the central hydrophilic proteoglycan-rich nucleus pulposus (NP), the concentric lamellar annulus fibrosus (AF), and two cartilaginous endplates (CEP) [11,12]. Due to severely limited vascularization up to the CEPs and outer AF, the IVD is the largest avascular structure in the human body, establishing a hypoxic microenvironment within the central areas of the disc [13]. As a consequence, the IVD exhibits a limited capacity for self-repair, resulting

* Corresponding author. Department of Orthopaedic Surgery, Surgical Science, Tokai University School of Medicine, 143 Shimokasuya, Isehara, Kanagawa, 259-1193, Japan.
E-mail address: daisakai@is.icc.u-tokai.ac.jp (D. Sakai).

https://doi.org/10.1016/j.redox.2024.103091
Received 26 January 2024; Accepted 14 February 2024
Available online 19 February 2024

in the gradual deterioration of the extracellular matrix (ECM). This progressive degradation encompasses a loss of overall cell density and cellular senescence and may promote inflammatory responses and increased catabolism [13]. The breakdown of ECM quality significantly compromises the biomechanical properties of the disc, limits diffusion of nutrients and gasses through the disc, thereby further exacerbating the degenerative process [14–16].

Oxidative stress is a ubiquitous biological phenomenon, occurring

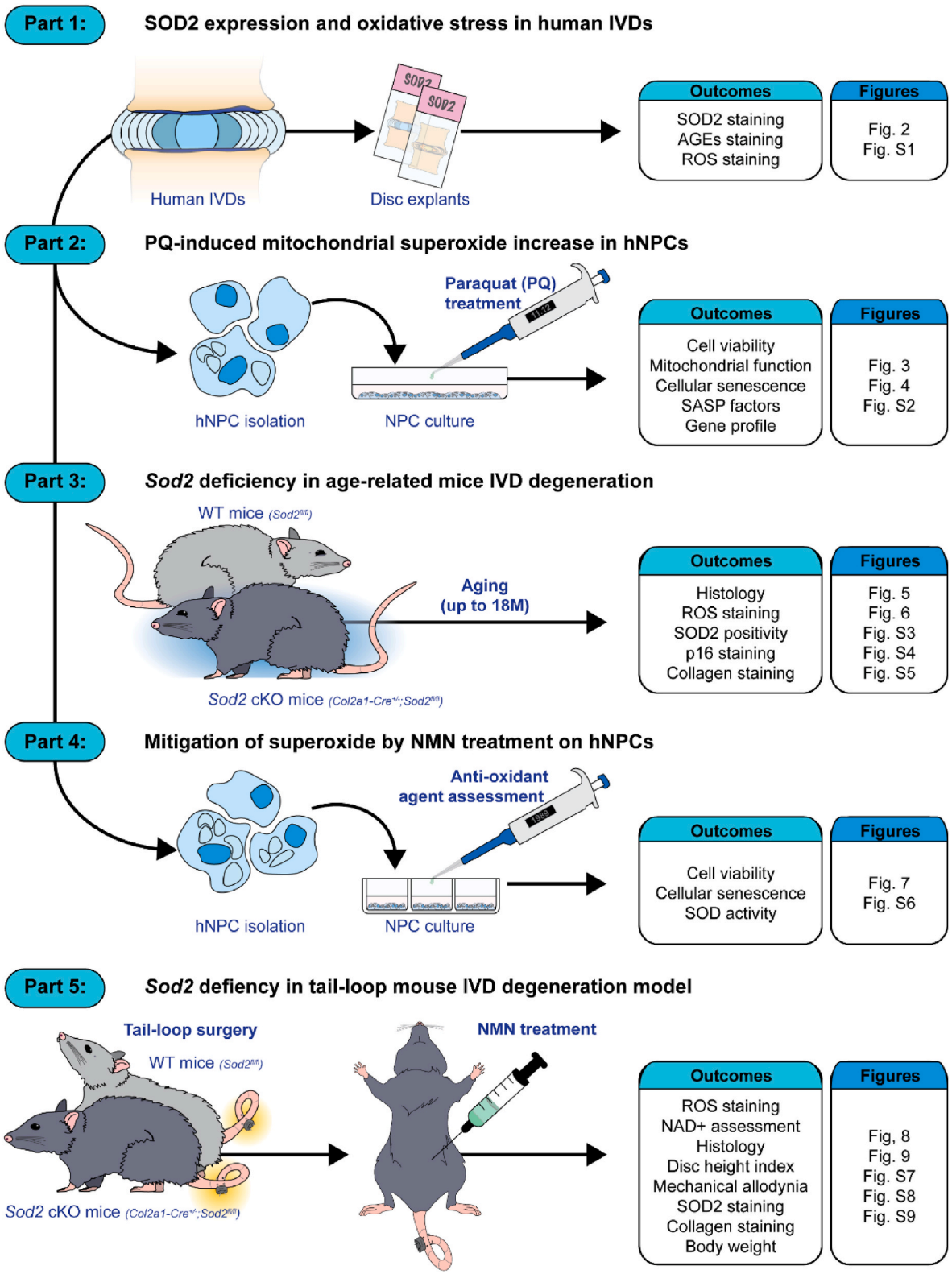

Fig. 1. Schematic representations of the experimental design and procedures. Abbreviations: AGEs – advanced glycation end products, cKO – conditional knockout, hNPC – human nucleus pulposus cell, IVD – intervertebral disc, NMN – β-nicotinamide mononucleotide, PQ – paraquat, ROS – reactive oxygen species, SASP – senescence-associated secretory phenotype, SOD2 – superoxide dismutase 2, WT – wild-type.

when the body's antioxidant mechanisms are overwhelmed by an excessive production and accumulation of reactive oxygen species (ROS). The oxidative imbalance can lead to cellular damage, affecting crucial components such as lipids, DNA, and proteins, thereby disrupting various physiological processes. Despite the hypoxic microenvironment within the IVD, NP cells (NPCs) are reported to consume a significant amount of oxygen to facilitate the production of ECM components [17–19]. Particularly noteworthy is the rich mitochondrial presence in NPCs, with intracellular ATP levels intricately tied to oxygen tension, irrespective of glucose concentration [17,20]. Paradoxically, numerous studies have indicated that central NPCs predominantly produce substantial amounts of lactic acid from glucose, suggesting an adaptability to anaerobic glycolysis rather than relying on the tricarboxylic acid (TCA) cycle for energy production [21,22]. This adaptability to anaerobic metabolism highlights the metabolic flexibility of NPCs, but remains generally poorly understood.

With that, emerging evidence strongly suggests that oxidative stress significantly contributes to IVD degeneration [23–26]. This complex phenomenon is intricately linked to the activities of crucial antioxidant enzymes, such as superoxide dismutase (SOD), catalase (CAT), and glutathione peroxidase-1 (Gpx-1) within the disc microenvironment. Here, superoxide dismutase 2 (SOD2) is a pivotal antioxidant enzyme that localizes in the mitochondria, a major site of ROS production. The primary role of SOD2 is to convert the toxic superoxide radicals, as a byproduct of cellular respiration, into oxygen and hydrogen peroxide to maintain the redox balance [27,28]. Mutations or altered expression of SOD2 have been implicated in various diseases, including neurodegenerative diseases, cardiovascular diseases, and cancer [29–33]. Reduced activity or expression of SOD2 may exacerbate oxidative damage, potentially accelerating the aging process or the onset of age-related diseases. We have previously demonstrated that *Sod2* deficiency in chondrocytes accelerates aging- and instability-induced cartilage degeneration in mice [34]. Despite aging being a significant risk factor for IVD degeneration, the specific role of SOD2 in IVD has remained elusive. We hypothesized that SOD2 plays an important role in maintaining redox homeostasis in IVD and that an imbalance between SOD2 and ROS accelerates IVD degeneration.

In this study (Fig. 1), we unveil a dual role of SOD2 in IVD health. Remarkably, our investigation reveals a nuanced pattern of SOD2 expression in human IVDs – upregulated during moderate degeneration but significantly downregulated in severe degenerative cases. Delving deeper, we identify a critical link between excessive mitochondrial superoxide and the acceleration of cellular senescence and ECM degradation in human NPCs. Equally experimental outcomes in mice showed that *Sod2* deficiency in IVDs not only accelerates age-related disc degeneration, but also exacerbates mechanical stress-induced degeneration. Moreover, SOD2 proved an excellent target to limit IVD degeneration, as we found that administration of β-nicotinamide mononucleotide (NMN), a subject of considerable research and public interest, could mitigate mechanical stress-induced IVD degeneration in mice. These findings, collectively, shed light on the intricate balance of redox dynamics in IVDs and present new avenues for targeted interventions against disc degeneration, but also provide insights that extend beyond the realm of IVD biology and offer valuable perspectives for understanding redox-related processes in various fields and pathologies.

2. Materials and methods

2.1. Human IVD tissue samples

All research procedures were approved by the Institutional Review Board for Clinical Research at Tokai University (application number 17R-173). All patients (or their legal guardians for those underaged) provided written informed consent for the collection and use of surgical waste for research purposes. Human IVD tissue samples were obtained from 21 patients (10 males and 11 females; 16–81 years of age) who underwent spine surgery at Tokai University Hospital and related institutions (Table S1). NP tissues were isolated and immediately cryopreserved. Half of the tissues were cryoembedded in Tissue-Tek optimal cutting temperature compound (Sakura Finetek, Tokyo, Japan) and sectioned into 7 μm thickness for immunohistochemical analysis and measurement of ROS, and the other half was used for western blotting and SOD activity analysis. IVD degenerative grades were classified by preoperative MRI according to the Pfirrmann grading system [35].

2.2. Isolation and culture of human NPCs

For in vitro study, human IVD-derived NPCs were isolated and cultured from 15 young patients (12 males and 3 females; mean age ± SD, 19.6 ± 3.4 years) undergoing surgery for lumbar disc herniation as described previously [36,37]. Briefly, the collected surgical NP tissue was washed with 0.9% saline and the tissue was cut into 3–5 mm in diameter pieces with scissors and scalpels. NP tissue fragments were directly seeded in complete culture medium containing Dulbecco's modified Eagle's medium (DMEM; Gibco, NY, USA) and α-minimal essential medium (αMEM; Gibco), supplemented with 20% (v/v) fetal bovine serum (FBS; Sigma-Aldrich, MO, USA) and 1% penicillin/streptomycin (Gibco) and cultured in 6-well polystyrene plates (IWAKI, Tokyo, Japan) at 37 °C in 5% CO_2 and physiologically relevant 5% O_2 levels [38] for 14 days without media replenishment. Subsequently, tissue fragments were collected, centrifuged, and the supernatant was removed. The tissue was then resuspended in TrypLE Express (Thermo Fisher Scientific, Tokyo, Japan) and digested at 37 °C for 30 min with gentle swirling. Next, the tissue was further digested in a mixture of αMEM supplemented with 10% (v/v) FBS and 0.25 mg/mL collagenase P (Roche, Basel, Switzerland), and incubated at 37 °C for 2 h. After digestion, the suspension was filtered through a 40 μm cell strainer (Corning, NY, USA), centrifuged, and the supernatant was removed. The resulting cells were seeded at 30,000 cells/dish in 100 mm tissue culture dishes (Corning) at 37 °C in 5% CO_2 and 5% O_2 and cultured in medium as previously specified for 7 days without media change. Human IVD-derived NPCs following the second passage were used for further in vitro experiments.

2.3. Paraquat treatment with/without antioxidants pretreatment

Paraquat (PQ; methyl viologen dichloride hydrate) is well known as a mitochondrial superoxide inducer [39,40]. To evaluate the effect of mitochondrial superoxide, a substrate for SOD2, NPCs were treated with PQ (856,177, Sigma-Aldrich) in αMEM supplemented with 10% (v/v) FBS for 24 or 48 h at 37 °C in 5% CO_2 and 5% O_2. Furthermore, to search for the potential compounds that can mitigate the cytotoxicity of PQ-induced mitochondrial superoxide on human NPCs, cells were pretreated with either 100 μM β-nicotinamide mononucleotide (NMN; 44501000, Oriental Yeast Co., Ltd, Tokyo, Japan), 50 μM N-acetylcysteine (NAC; A8199, Sigma-Aldrich), 100 μM L-ascorbic acid (AA; A4544, Sigma-Aldrich), 100 μM L-ascorbic acid 2-phosphate sesquimagnesium salt hydrate (AA2P; A8960, Sigma-Aldrich), 20 μM ferulic acid (FA; 4-hydroxy-3-methoxycinnamic acid, 90,034, Sigma-Aldrich), 20 μM *trans*-ferulic acid (t-FA; 128,708, Sigma-Aldrich), or 50 μM MitoTEMPO (MT; SML0737, Sigma-Aldrich) for 2 h, and then treated with PQ for 24 h. The concentration of each compound was determined based on the cell viability assay at the concentration that retained the most cell viability (Fig. S6).

2.4. Animals

All animal studies were performed in accordance with protocols approved by the Institutional Animal Care and Use Committee of Tokai University (211,075, 222,004, 233,006 and 231,121), and adhered to

institutional and national guidelines for animal experiments. *Col2a1-Cre*$^{+/-}$ transgenic mice on a C57BL/6J background [41] and *Sod2*$^{fl/fl}$ mice on a C57BL/6NCrSlc background [42] were kindly provided by Dr. Takahiko Shimizu (National Center for Geriatrics and Gerontology, Obu, Japan). These mice were crossed to generate chondrocyte-specific *Sod2* conditional knockout (cKO) mice (*Col2a1-Cre*$^{+/-}$*; Sod2*$^{fl/fl}$) as described previously [34]. The primer sequences used for genotyping are shown in Table S2. 15-week-old male Sprague-Dawley rats (n = 6) were obtained from CLEA Japan (Tokyo, Japan). All animals were housed under specific pathogen-free conditions at room temperature (23 ± 2 °C) with a 12-h light/dark cycle and ad libitum access to food and water.

2.5. Age-related spontaneous IVD degeneration model

Lumbar and caudal IVD of 6-month-old (6 M; healthy young), 12-month-old (12 M; middle-aged), and 18-month-old (18 M; aged) *Sod2*$^{fl/fl}$ (for convenience, referred to as wild-type; WT) and *Col2a1-Cre*$^{+/-}$; *Sod2*$^{fl/fl}$ (*Sod2* cKO) mice were analyzed. These time points were determined based on previous studies showing progressive morphological changes in the lumbar IVD of mice aged 14 months or older [43]. The number of mice from each sex in each age group was as follows; 6 M: WT: 4 females, 2 males; *Sod2* cKO: 3 females, 3 males; 12 M: WT: 5 females, 1 male; *Sod2* cKO: 3 females, 3 males; 18 M: WT: 4 females, 2 males; *Sod2* cKO: 3 females, 3 males. Mice were euthanized by cervical dislocation, and all lumbar IVDs (L1-S1) and proximal coccygeal IVDs (Co2-5) were harvested for evaluation. L1/2 and L2/3 IVDs were prepared for fresh frozen sections in the axial plane at 7 μm thickness and evaluated for measurement of intracellular and mitochondrial ROS. L3/4-L6/S1 and Co2/3-Co4/5 IVDs were used for histopathological and immunohistochemical analysis.

2.6. Mechanical stress-induced IVD degeneration model by tail-looping

We used the tail-looping model to induce IVD degeneration by uneven mechanical load as a modification of our previously reported method [44]. Mice were placed in the supine position and anesthetized with 2.0% isoflurane. The IVD level was confirmed by palpation and fluoroscopy, and the distal tail portion was excised at Co13/14 level. One 23G needle was inserted into the Co13 vertebra and two 23G needles were inserted into the Co5 vertebra from the lateral side of the tail, and 0.3 mm stainless steel wire was passed through the needle holes. To facilitate biological wound healing, a small skin incision, approximately the same size of the Co13/14 distal resection edge was made on the lateral surface of the Co5 vertebra. The tail was looped laterally in a fixed position between the Co5 and Co13 vertebrae, and the loop was held in place with a small aluminum sleeve (Fig. 8A). Subsequently, 0.1 mg/kg lepetan (buprenorphine HCL; Otsuka Pharmaceutical, Japan) was administered for postoperative analgesia, and body weight was monitored weekly throughout the study. This IVD compression model provides relatively constant compression in all mice due to minimal surgical variability. Co2/3 and Co3/4 IVDs were analyzed as the non-degenerative control group (Group C). Co7/8, Co8/9, Co9/10, and Co10/11 IVDs were analyzed in the degenerative IVD group (Group TL).

Six 15-week-old male WT mice were used to assess mitochondrial ROS in the IVD following mechanical stress by tail-looping. Mice were euthanized 24 h after tail-looping surgery, and dissected spines were prepared for fresh frozen sections in the coronal plane at 7 μm thickness.

To evaluate the therapeutic potential of NMN for IVD degeneration induced by the tail-looping model in WT and *Sod2* cKO mice, 15-week-old male mice were injected intraperitoneally with NMN (500 mg/kg of body weight; dissolved in 0.2 mL phosphate-buffered saline (PBS)) or PBS (0.2 mL per injection) twice weekly starting 1 week before surgery until euthanasia. NMN concentrations were based on a previous study [45]. A total of 16 *Sod2* cKO and 16 WT mice were randomly assigned to either NMN or PBS treatment, resulting in the following groups: WT mice treated with PBS (WT + PBS group), WT mice treated with NMN (WT + NMN group), cKO mice treated with PBS (cKO + PBS group), and cKO mice treated with NMN (cKO + NMN group) (n = 8 mice per group). All mice were euthanized at 4 weeks after tail-looping surgery for histopathological and immunohistochemical analysis (Fig. 8C).

2.7. Histology

Dissected spines were fixed in 10% neutral buffered formalin for 48 h, decalcified in 0.5 M EDTA (pH 7.4) for 2 weeks, and embedded in paraffin. Mid-sagittal sections for lumbar IVDs and mid-coronal sections for coccygeal IVDs were cut into 5 μm thickness and stained with hematoxylin/eosin (H&E) and safranin-O/fast green. Morphological changes were evaluated and scored in a blinded manner according to the Orthopaedic Research Society (ORS) spine mouse-specific standardized histopathology scoring system [46].

2.8. Immunohistochemistry

Human IVD fresh frozen sections and mouse paraffin sections were used for immunohistochemistry. Cryosections and deparaffinized sections following antigen retrieval were treated with 0.3% H_2O_2/methanol for 30 min to block endogenous peroxidase activity. The sections were then blocked in 5% normal goat serum in PBS for 30 min and incubated overnight at 4 °C with primary antibodies against SOD2 (1:100 for human and mouse lumbar IVD, 1:1000 for mouse coccygeal IVD, ab13534, Abcam, Cambridge, UK), AGEs (1:100, ab23722), collagen II (1:100, ab34712), and p16^{INK4a} (1:250 for mouse lumbar IVD, 1:1000 for mouse coccygeal IVD, ab108349). For the negative control, the primary antibody was replaced with normal rabbit IgG isotype control (X0936, Dako, Agilent Technologies, CA, USA). Subsequently, the sections were reacted with Histofine Simple Stain MAX PO (R) (Nichirei Biosciences, Tokyo, Japan) for 1 h at room temperature, and the color was visualized with Simple Stain DAB (3,3′-diaminobenzine) Solution (Nichirei Biosciences) and counterstained with hematoxylin. Images were visualized with a fluorescence microscope (BZ-9000, Keyence, Osaka, Japan). For the detection of SOD2 and p16^{INK4a}, heat mediated antigen retrieval was performed with Tris/EDTA buffer (pH 9.0, S2367, Dako) for 10 min at 98 °C. For the detection of collagen II (COL2), enzyme antigen retrieval was performed with proteinase K (S3020, Dako) for 5 min at room temperature. The percentage of SOD2-and p16^{INK4a}-positive cells was counted manually, and the percentage of AGEs- and COL2-positive areas was measured automatically using the color deconvolution plugin in ImageJ/Fiji software (National Institutes of Health), as described previously [47]. For the percentage of COL2-positive area, the boundaries of the NP and AF were digitally traced using the freehand tool, and then images with selected ROI of NP area were calculated.

2.9. Protein extraction

Human NP tissues were homogenized using a Shake master NEO (Biomedical science, Tokyo, Japan) with two stainless steel beads twice for 3 min at 1500 rpm at 4 °C in RIPA buffer (9806, Cell Signaling Technology (CST), MA, USA) containing PMSF (8553, CST). Human NPCs were washed with TBS and lysed in RIPA buffer containing PMSF. Soluble proteins were sonicated on ice using a Bioruptor II (BM Equipment Co., Ltd, Tokyo, Japan) and centrifuged at 14,000 rpm for 10 min at 4 °C. Protein concentrations were quantified using the DC protein assay kit (Bio-Rad, CA, USA).

2.10. Capillary electrophoresis-based western blotting

Capillary electrophoresis-based western analysis was performed using a Wes instrument (ProteinSimple, CA, USA) according to the manufacturer's instructions. Protein samples (10 μg/lane) were diluted with 0.1 × sample buffer and mixed with 5 × fluorescent master mix in a

4:1 ratio. The mixed samples were heated at 95 °C for 5 min. Primary antibodies were diluted with antibody diluent II for SOD2 (1:50, ab13534), p53 (1:50, sc-126, Santa Cruz Biotechnology, Texas, USA), p21 (1:50, 2947, CST), $p16^{INK4a}$ (1:25, ab108349), GAPDH (1:100, G9545, Sigma-Aldrich), and β-actin (1:500, A5441, Sigma-Aldrich). Secondary antibodies were used according to the manufacturer's instructions: anti-mouse HRP conjugated secondary antibody (042–205, ProteinSimple) and anti-rabbit HRP-conjugated secondary antibody (042–206, ProteinSimple). The size-based assay was then performed automatically on the Wes instrument (SM-W004, ProteinSimple). The capillaries were loaded with separation matrix for 200 s, stacking matrix for 15 s, and sample for 9 s. Separation was then performed at 375 V for 25 min in each capillary. After separation, the capillaries were exposed to ultraviolet light for 200 s and then washed with wash buffer. After blocking with antibody diluent buffer for 5 min, the capillaries were incubated with primary and secondary antibodies for 30 min, respectively. Finally, the signal was detected by chemiluminescence with luminol-S (043–311, ProteinSimple) and peroxide (043–379, ProteinSimple) and calculated by Compass software.

2.11. SOD activity assay

The protein lysate from human NP tissue and cultured NPCs was used for SOD activity assay using the SOD Assay Kit - WST (S311, Dojindo, Kumamoto, Japan) according to the manufacturer's instructions. Results were expressed as units per mg protein.

2.12. Measurement of intracellular and mitochondrial ROS

Fresh frozen sections from human NP tissues and mouse IVD tissues were used for measurement of ROS. Intracellular and mitochondrial superoxide levels were evaluated using dihydroethidium (DHE; Invitrogen, MA, USA) and MitoSOX Red Mitochondrial Superoxide Indicator (Invitrogen), respectively. The sections were incubated with 10 μM DHE or 5 μM MitoSOX at 37 °C for 30 min under protection from light, and then nuclei were counterstained with DAPI. Fluorescence staining was analyzed by confocal microscopy (LSM700, Carl Zeiss, Oberkochen, Germany) with an excitation wavelength of 555 nm and an emission wavelength of 573 nm. The mean fluorescence intensity (MFI) in the NP and AF was quantified using Image J.

For the measurement of ROS levels in cultured cells, NPCs were washed three times with PBS, and incubated with 10 μM DHE or 5 μM MitoSOX at 37 °C for 30 min in the dark. Cells were analyzed by flow cytometry using BD FACS Canto II (BD Biosciences, NJ, USA) as described previously [37]. MFI of DHE and MitoSOX was measured by FACS through phycoerythrin (PE) with an excitation wavelength of 488 nm and an emission wavelength of 578 nm.

2.13. Cell viability assay

Cell viability was determined using the Cell Counting Kit-8 (CCK-8; CK04, Dojindo) according to the manufacturer's instructions. After PQ treatment with/without antioxidant pretreatment, 10 μL CCK-8 solution was added to each well, and the cells were further cultured at 37 °C for 4 h. Absorbance in the wells was measured at 450 nm using the GloMax Discover Microplate Reader (Promega, WI, USA). Cell viability was expressed as percentage of control values set at 100%.

2.14. Apoptosis analysis

Apoptotic and necrotic cells were measured by flow cytometry using the APC Annexin V Apoptosis Detection Kit with propidium iodide (PI; BioLegend, CA, USA) as described previously [37]. Briefly, after PQ treatment, cells were washed three times with PBS, and resuspended in 100 μL of Annexin V binding buffer, supplemented with 5 μL of Annexin V and 5 μL of PI. Samples were incubated for 15 min at room temperature in the dark. Viability (Annexin-V^-/PI^-), apoptosis (Annexin-V^+), and necrosis (Annexin-V^-/PI^+) rates were analyzed using BD FACS Canto II.

2.15. Mitochondrial membrane potential analysis

Mitochondrial membrane potential was measured by flow cytometry using the JC-1 MitoMP Detection Kit (MT09, Dojindo) according to the manufacturer's instructions. After PQ treatment, cells were washed three times with PBS, and incubated with 2 μM JC-1 working solution at 37 °C for 30 min in the dark. Results were expressed as red/green fluorescence intensity ratio.

2.16. NPC surface marker and ECM analysis

NPC surface markers were analyzed by flow cytometry as described previously [48]. After PQ treatment, cells were washed three times with PBS, and incubated on ice for 1 h in the dark with antibodies against APC-conjugated Tie-2 (FAB3131A, R&D Systems, MN, USA), PE-conjugated GD2 (562,100, BD Biosciences), and FITC-conjugated CD24 (555,427, BD Biosciences). For the isotype control, the antibody was replaced with IgG1 mouse APC (IM2475, Beckman Coulter, CA, USA), IgG1 mouse PE (A07796, Beckman Coulter), and IgG1 mouse FITC (A07795, Beckman Coulter). Only viable cells were analyzed using the PI-negative gate.

For ECM analysis, cells were fixed and permeabilized with IntraPrep Permeabilization Reagent (A07803, Beckman Coulter). Cells were then subjected to three cycles of freezing (−80 °C) and thawing (37 °C). Subsequently, cells were incubated overnight at 4 °C with primary antibodies against collagen II (NB600-844, Novus Biologicals, CO, USA) and proteoglycan (MAB2015, Sigma-Aldrich). After washing with PBS, cells were reacted with goat anti-mouse Alexa Flour 488-conjugated secondary antibody (A28175, Invitrogen) on ice for 1 h in the dark, and then analyzed by flow cytometry.

2.17. Transmission electron microscopy

NPCs were plated at 10,000 cells/dish in 35 mm tissue culture dishes. After 72 h, cells were treated with PQ (10 mM and 30 mM) for 24 h. Cells were fixed with 2.5% glutaraldehyde in 0.05 M phosphate buffer (pH 7.3) for 1 h at room temperature, and then post-fixed with 1% osmium tetroxide in the same buffer for 1 h at room temperature. After dehydration through a graded ethanol series, cells were embedded in Quetol 812 (Nisshin EM Co., Tokyo, Japan). Ultrathin sections (90 nm) were cut using an EM UC7 ultramicrotome (Leica Microsystems), post-stained with uranyl acetate and lead citrate, and visualized with a transmission electron microscope (JEM-1400; JEOL, Tokyo, Japan).

2.18. Cell proliferation

NPCs were seeded at 30,000 cells/dish in 100 mm tissue culture dishes. After 72 h, cells were treated with PQ for 48 h, and then harvested using TrypLE Express at 37 °C for 5 min. Subsequently, the number of viable cells was counted with Trypan blue solution 0.4% (Gibco) under a phase contrast microscope (ECLIPSE Ti2, Nikon). Cell proliferation rate (fold increase) was calculated as the number of cells at the time of collection/30,000 cells (seeded cells).

2.19. Senescence-associated β-galactosidase staining

Senescence-associated β-galactosidase (SA-β-Gal) staining was performed to detect senescent cells using the Senescence β-galactosidase Staining Kit (9860, CST). After PQ treatment with/without antioxidant pretreatment, cells were washed three times with PBS, and fixed with 1 × fixative solution for 10 min at room temperature. After washing with PBS, cells were incubated with β-Gal staining solution at 37 °C for 24 h at

pH 6.0. Images were visualized with an ECLIPSE Ti2 microscope (Nikon, Tokyo, Japan). The percentage of SA-β-Gal positive cells was calculated in three random fields per biological replicate.

2.20. qRT-PCR

Total RNA was extracted from cultured NPCs using ISOGEN II (Nippon Gene, Tokyo, Japan) according to the manufacturer's instructions. cDNA was synthesized from 300 ng of total RNA using the High-Capacity RNA to cDNA Kit (4387406, Applied Biosystems, Thermo Fisher Scientific). Real-time PCR was performed with TaqMan Fast Advanced Master Mix (4444556, Applied Biosystems) using an amplification machine (QuantStudio 3; Applied Biosystems) with stage 1 (95 °C for 20 s × 1 cycle) and stage 2 (95 °C for 1 s, 60 °C for 20 s × 40 cycles). Sample values were normalized by the Ct value for the housekeeping gene GAPDH. The Ct value of the control was used as a reference, and then relative mRNA expression was calculated using the $2^{-\Delta\Delta Ct}$ method. The TaqMan probe & primers used for qRT-PCR are listed in Table S3.

2.21. Enzyme-linked immunosorbent assay (ELISA)

The concentration of inflammatory mediators (IL-6, IL-1β) in the supernatant of the cell culture medium collected after 48 h treatment with PQ was measured by enzyme-linked immunosorbent assay according to the manufacturer's instructions (R&D Systems, cat: D6050B, DLB50).

2.22. NAD^+ measurement

NAD^+ levels were measured with a NAD/NADH Assay Kit (N509, Dojindo) according to the manufacturer's instructions. 3–6 month old *Sod2* cKO mice were injected intraperitoneally with NMN (500 mg/kg of body weight), and vertebra-IVD-vertebra units of the coccygeal spine were harvested at 0, 1, 3, and 6 h after injection (n = 3 mice per time point). Furthermore, 15-week-old Sprague-Dawley rats were injected intraperitoneally with NMN (500 mg/kg of body weight), and coccygeal IVDs were harvested at 0 and 3 h after injection (n = 3 rats per time point). After washing with pre-cooled PBS, the tissue was weighed and homogenized with NAD^+/NADH extraction buffer. After centrifugation, the supernatant was used as the assay sample. Total NAD^+/NADH and NADH levels were quantified by a colorimetric assay at 450 nm using the VersaMax Microplate Reader (Molecular Devices, CA, USA). The NAD^+ concentration was calculated by subtracting the NADH values from the total NAD^+/NADH.

2.23. Radiographic analysis

Frontal radiographs of the tail were taken from all mice under general anesthesia before, 0, 2, and 4 weeks after tail-looping surgery using a fluoroscopic image intensifier (DHF-105CX, Hitachi, Tokyo, Japan). We defined the convex/concave disc height index (DHI) ratio as shown in Fig. 8F, and measured the Co 8/9 and Co 9/10 levels using Image J in a blinded manner. Changes in the DHI were expressed as %DHI and normalized to the preoperative DHI (%DHI = [postoperative DHI/preoperative DHI] x 100), as described previously [49].

2.24. Animal behavioral nociceptive tests

The von Frey test was performed 3 days before surgery (day −3) and on days 3, 7, 14, and 27 after surgery using a dynamic plantar aesthesiometer (Ugo Basile Biological Instruments, Gemonio, Italy). Mice were placed into individual compartments with wire mesh floors and lids with air holes, and were habituated to the test environment for 30 min prior to the tests to minimize exploratory activity. The filaments were applied to the hind paw, base of the tail, and looped tail on the ventral surface with a linear increase in force from 0 to 5 g over 10 s and then constant force at 5 g for 20 s, as described previously [50]. Withdrawal latency and force were recorded as sensory thresholds when the mice showed nociceptive responses. The test was repeated four times for each mouse and the results were expressed as the mean of the multiple measurements. All behavioral tests were performed by the same blinded investigator.

2.25. Statistics

All statistical analyses were performed using GraphPad Prism version 9.5.1 (GraphPad Software, CA, USA). Data are expressed as mean ± SD. Data distribution was assessed by the Shapiro-Wilk test for normality. Differences between the two groups were analyzed by two-tailed unpaired Student's t-test. Differences between multiple groups were analyzed by one-way or two-way ANOVA, followed by Tukey's multiple comparisons test. Non-normally distributed data were analyzed by Kruskal-Wallis, followed by Dunn's multiple comparisons test. $P < 0.05$ was considered a statistically significant difference. The sample size for each experiment was determined based on our previous experience and literature using similar methods had reported moderate effect sizes. All in vitro experiments were performed on at least three independent patient samples with at least two technical replicates. All in vivo experiments were performed on at least three biologically independent animals in each group.

3. Results

3.1. SOD2 levels are linked with severity of disc degeneration

As a preliminary investigation into the role of SOD2 in IVD degeneration, we examined SOD2 expression and oxidative stress markers in human IVD tissue samples obtained from patients undergoing spine surgery (Table S1). Immunohistochemical analysis revealed a low expression of SOD2 in Pfirrmann grade II (mild degeneration), which increased with the progression of IVD degeneration (Fig. 2A and B). The expression of advanced glycation end products (AGEs) [51], an oxidative damage marker, also showed increased positivity rates with the progression of disc degeneration (Fig. 2A and B). Notably, SOD2 and AGEs positivity showed a strong significant positive correlation with patient age (Fig. 2B) and Pfirrmann grade (Fig. S1). Western blot results validated a significant increase in the level of SOD2 for moderate degeneration (Pfirrmann grade III), but showed a decrease for more severe degeneration (Pfirrmann grade IV) (Fig. 2C). Protein levels of SOD2 showed a significant correlation with an increase in age (Fig. 2D). Considering the decrease in cell numbers and their activity with disc degeneration, and considering that SOD activity is regulated by post-translational modifications [52], we assessed the total SOD activity, revealing again a significant increase in SOD activity for moderate degeneration, followed by a decrease for severe disc degeneration (Fig. 2E). Next, intracellular and mitochondrial superoxide levels were respectively evaluated using DHE and MitoSOX fluorescence staining. MFI of DHE was 1.64-fold higher in grade III and 2.56-fold higher in grade IV compared to grade II. Similarly, MFI of MitoSOX was 2.02-fold higher in grade III and 2.61-fold higher in grade IV compared to grade II (Fig. 2F). These results thus indicate an increase in oxidative stress with human disc degeneration, which is marked by an increase in SOD activity for moderate degeneration, but might be decompensated for severe degeneration.

3.2. PQ treatment promotes excessive superoxide production, apoptosis, and mitochondrial dysfunction in human NPCs

The effects of mitochondrial superoxide, a substrate of SOD2, on cultured human NPCs were examined through treatment with PQ, a well-known mitochondrial superoxide inducer [39,40]. Phase contrast

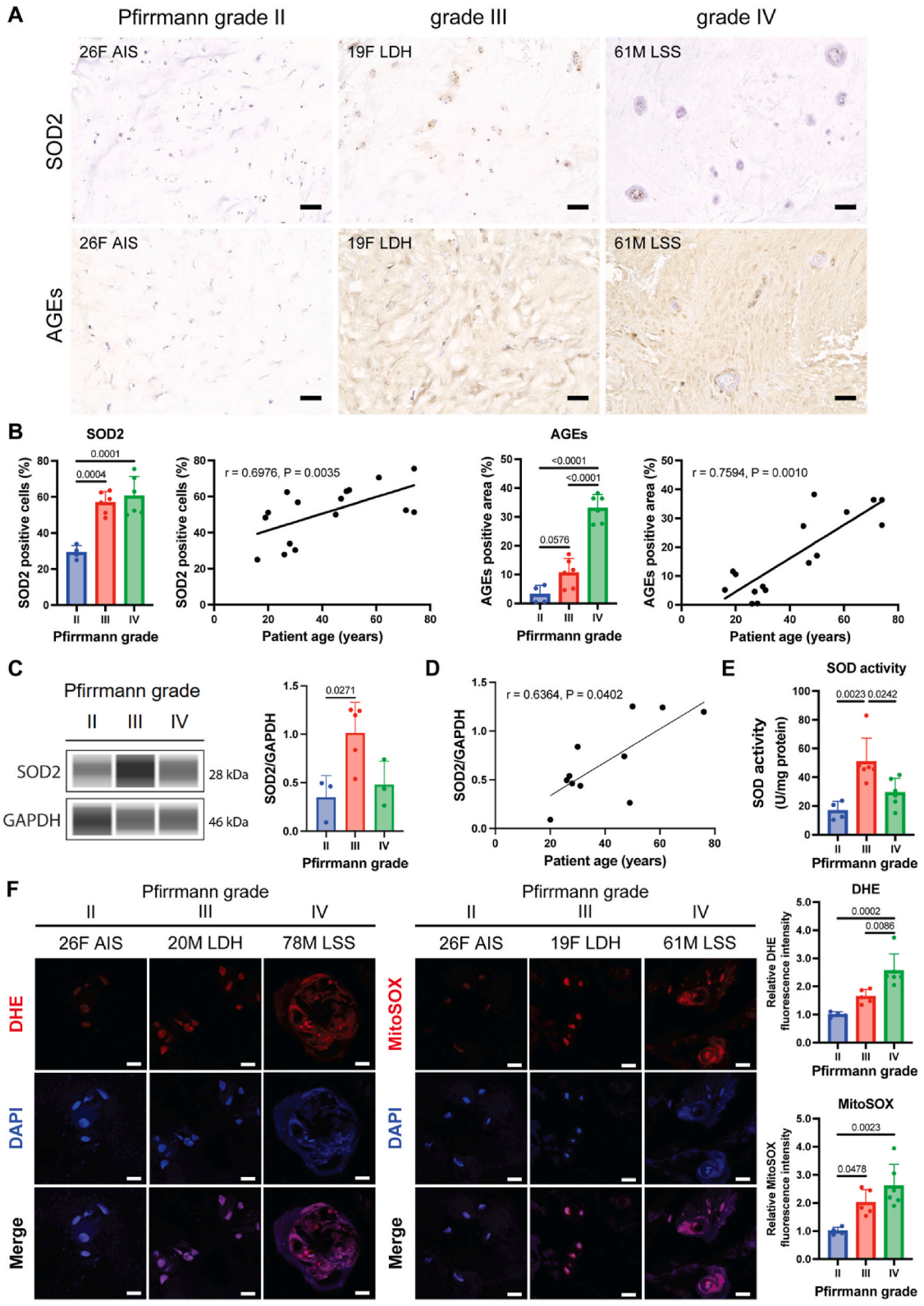

Fig. 2. Expression of SOD2 and oxidative stress markers in human IVD. (A) Immunohistochemistry of SOD2 and AGEs in human IVD with each degenerative grade. Scale bars, 100 μm. (B) Quantification of the rates of SOD2-positive cells and AGEs-positive area. Spearman's rank correlation coefficient between SOD2 positivity or AGEs positivity and patient age. (C) Western blot example and graphical representation of SOD2 in total protein extracts isolated from human IVD tissue with each degenerative grade. GAPDH was used as a loading control. (D) Spearman's rank correlation coefficient of SOD2 protein levels with age of donor sources. (E) SOD activity in total protein extracts isolated from human IVD tissue with each degenerative grade. (F) DHE and MitoSOX fluorescence staining in human IVD with each degenerative grade and quantification of mean DHE and MitoSOX fluorescence intensity. Scale bars, 20 μm. (B, C, E, F) Data are expressed as mean ± SD. In B, E (n = 4 for grade II, n = 6 for grade III and n = 6 for grade IV), in C (n = 3 for grade II, n = 5 for grade III and n = 3 for grade IV) and in F (n = 4 for grade II, n = 5 for grade III and n = 6 for grade IV), one-way ANOVA, followed by Tukey's multiple comparisons test was used for statistical analysis. Abbreviations: AIS – adolescent idiopathic scoliosis, LDH – lumbar disc herniation, LSS – lumbar spinal stenosis.

microscopy revealed a dose-dependent reduction in cell density, coupled with enlarged and flattened cell morphology, a typical characteristic of senescent cells (Fig. 3A). Furthermore, PQ treatment led to a significant decrease in cell viability and a significant increase in apoptosis rates, both in a dose-dependent manner (Fig. 3B–D). Consistent with ex vivo analysis, MFI of DHE and MitoSOX increased in response to PQ in a dose-dependent manner (Fig. 3E). Specifically, MitoSOX MFI increased 2.00-fold at 10 mM PQ and 2.49-fold at 30 mM PQ compared to untreated controls, matching the results of ex vivo results for moderate degeneration (Pfirrmann grade III) and severe degeneration (grade IV) samples. Considering the overall findings, we selected 10 mM PQ as a representative model for moderate degeneration and 30 mM PQ for severe degeneration in our subsequent experiments. Next, transmission electron microscopy revealed that control cells exhibited a relatively juvenile appearance with some small notochordal cell-like vacuoles [53] remaining and the presence of plenty mitochondria with normal morphology. Conversely, cells treated with 10 mM PQ showed a mixture of both normal mitochondria and swollen mitochondria with disrupted cristae, while cells treated with 30 mM PQ displayed shrunken mitochondria with ruptured outer membranes (Fig. 3F). Furthermore, mitochondrial membrane potential, assessed through JC-1 staining, demonstrated a significant decrease in a PQ dose-dependent manner (Fig. 3G).

3.3. Excessive mitochondrial superoxide leads to progenitor cell depletion and cellular senescence

We further explored the impact of mitochondrial superoxide on human NPCs. We previously identified angiopoietin-1 receptor (Tie2) and disialoganglioside 2 (GD2) as markers for NP progenitor cells, characterized by their robust multipotency and high self-renewal capacity [54]. However, this cell populations declines rapidly with age and the progression of degeneration [54]. Alternatively, CD24 serves as a specific marker for healthy yet mature NPCs [54,55]. PQ treatment showed a strong reduction in the Tie2 and GD2 positivity rates, while CD24 positivity demonstrated an initial increase at 10 mM PQ, which subsequently decreased at higher concentrations (Fig. 4A and Figs. S2A–C). These findings suggest initial cellular attempts to counteract the mild degenerative oxidative stress, but an inability to respond effectively at higher concentrations. We then assessed the active production of key NP-ECM components i.e., COL2 and proteoglycan (PG), through flow cytometry. Upon PQ treatment, we observed a significant reduction in the percentage of NPCs actively producing COL2, indicating a disruption in the synthesis of essential ECM components, although, the proportion of cells producing PG remained unaffected. (Fig. 4B and Figs. S2D and E).

Next, we examined the correlation between mitochondrial superoxide and NPCs senescence. A dose-dependent increase in the rate of SA-β-Gal positive cells was observed, accompanied by a decrease in cell proliferation rates (Fig. 4C and D). Cellular senescence is mainly divided into replicative senescence, which is regulated by the p53-p21 pathway in a telomere-dependent manner, and stress-induced premature senescence, which activates the $p16^{INK4a}$ pathway [25,56,57]. Western blotting showed that the activation of both p53-p21 and $p16^{INK4a}$ pathways was enhanced in a PQ dose-dependent manner (Fig. 4E and F). Interestingly, both SOD2 protein expression levels and SOD activity were enhanced at low PQ concentrations and decreased at higher concentrations (Fig. 4E, F, H). Cellular senescence is a regulated process which involves not only proliferation arrest, but also the alteration of the gene expression patterns, collectively known as the senescence-associated secretory phenotype (SASP), which includes an upregulation in the secretion of pro-inflammatory cytokines and matrix proteases [58,59]. Thus, we further aimed to characterize the senescent state of treated NPCs by evaluating the gene expression of ECM anabolic markers, ECM catabolic markers, and inflammatory cytokines after PQ treatment in relation to the expression of antioxidant enzymes. Interestingly, *SOD1*, *SOD2* and *GPX1* gene expression were upregulated, while *SOD3* and *CAT* gene expression were downregulated by PQ-treatment (Fig. 4G). As expected, ECM anabolic factors (*COL2A1* and *ACAN*) were significantly downregulated, whereas catabolic factors (*MMP13* and *ADAMTS5*) as well as inflammatory cytokines (*TNFA*, *IL1B* and *IL6*) were significantly upregulated in PQ-treated NPCs (Fig. 4I and J). Furthermore, the ELISA results confirmed a significant increase in the inflammatory cytokines IL-1β and IL-6 in the culture medium collected after PQ treatment (Fig. 4K). Taken together, excessive mitochondrial superoxide production in human NPCs, induced by PQ treatment, depletes progenitor cells, triggers cellular senescence, and upregulates SASP factors linked to IVD degeneration associated with matrix degradation and inflammation.

3.4. Sod2 deficiency in IVD accelerates age-related IVD degeneration in mice

To investigate whether *Sod2* deficiency in IVD affects the progression of age-related IVD degeneration in vivo, we used chondrocyte-specific *Sod2* cKO mice (*Col2a1-Cre*$^{+/-}$; *Sod2*$^{fl/fl}$) as described previously [34]. Lumbar and coccygeal IVDs of 6 M (healthy young), 12 M (middle-aged), and 18 M (aged) *Sod2*$^{fl/fl}$ (WT) and *Sod2* cKO mice were analyzed. No significant differences in body weight or general health were observed between WT and *Sod2* cKO mice during aging (Fig. S3C). Immunohistochemical results confirmed the successful deletion of SOD2 in both lumbar and coccygeal discs, as indicated by the complete loss of SOD2 positive cells in NP, AF and EP regions. Contrary to the results in human IVD tissue, SOD2 positivity in lumbar and coccygeal IVD of WT mice decreased with aging (Figs. S3D and E).

Next, we evaluated intracellular and mitochondrial superoxide levels in lumbar IVD at 6 M, 12 M, and 18 M for both WT and *Sod2* cKO mice. We observed a gradual increase of DHE MFI in NP and AF regions of WT mice at 12 M and 18 M compared to 6 M, resulting in a 1.27-fold and 1.63-fold increase at 18 M for NP and AF tissues, respectively (Fig. 5A–C). MFI of MitoSOX exhibited a similar trend in WT mice with NP presenting a 1.69-fold increase and the AF region showing a 2.02-fold increase at 18 M compared to 6 M (Fig. 5B–D). Again, these results emphasize the presence of a natural accumulation of oxidative stress in the IVD with aging. The increase in DHE and MitoSOX MFI was significantly enhanced in *Sod2* cKO mice, demonstrating significantly higher oxidative stress levels compared to WT mice at all time points of sacrifice. Specifically, DHE MFI in the NP and AF were 1.84-fold and 1.48-fold higher, respectively, than the WT mice at 18 M, and similarly, MitoSOX MFI were 1.86-fold and 1.35-fold higher in the *Sod2* cKO mice (Fig. 5A–D).

Further histological analysis revealed that *Sod2* deficiency and superoxide accumulation accelerated age-related spontaneous IVD degeneration in both lumbar and coccygeal IVDs (Fig. 5E). Specifically, the WT mice showed only mild IVD degeneration at 18 M (mean total score; lumbar: 10.3, coccygeal: 9.6), whereas the *Sod2* cKO mice displayed significantly expedited IVD degeneration with a mean total score of 17.1 and 17.2 for lumbar and coccygeal discs, respectively, indicating moderate degeneration (Fig. 5E, F and Fig. S4). Notably, we observed elevated superoxide in the IVD at 12 M in WT mice, preceding histologically evident disc degeneration (observed at 18 M in WT mice). This suggests that oxidative stress accumulation may precede macroscopic degenerative changes, emphasizing it as a promising therapeutic target.

Furthermore, $p16^{INK4a}$ positivity in the lumbar and coccygeal IVD of WT mice tended to increase slightly with age, whereas $p16^{INK4a}$ positivity in *Sod2* cKO mice was significantly higher than that of WT mice from 6 M of age (Fig. 6A and Fig. S5), confirming that both age and *Sod2* deficiency significantly promote cellular senescence. COL2 positivity tended to decrease with age in both types of mice, but *Sod2* cKO mice exhibited significantly lower COL2 positivity than WT mice at 18 M of age (Fig. 6B). Overall, these results establish a direct link between *Sod2* deficiency, heightened oxidative stress, and accelerated age-related IVD degeneration. Notably, the observed increase in superoxide levels at 12

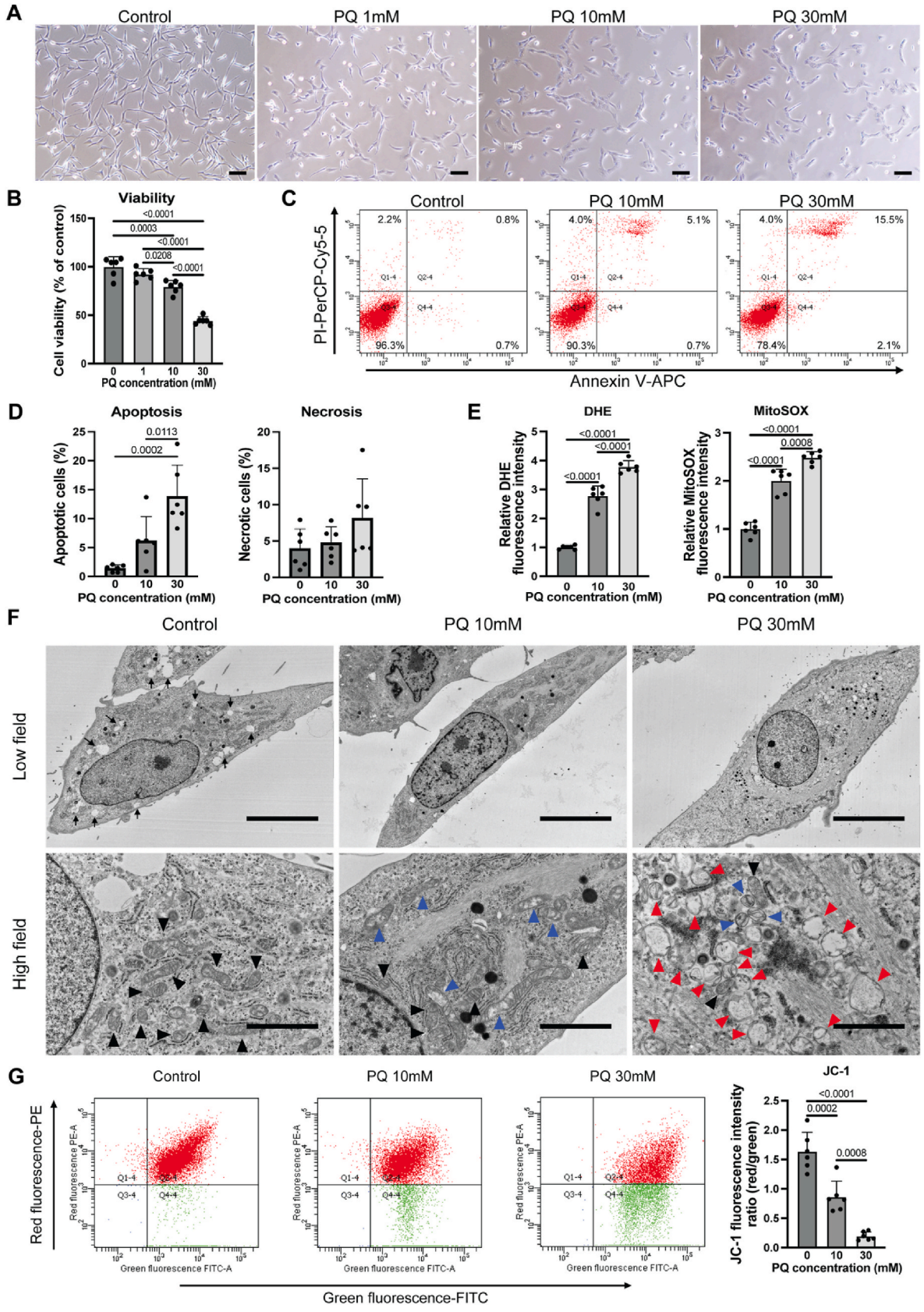

(caption on next page)

Fig. 3. PQ treatment promotes excessive superoxide production, apoptosis, and mitochondrial dysfunction in human NPCs. (A) Representative phase contrast microscopic images of human NPCs after 24 h treatment with PQ. Scale bars, 100 μm. (B) Cell viability of human NPCs after 24 h treatment with PQ. (C, D) Representative flow cytometry graphs of Annexin V/PI staining of human NPCs after 24 h treatment with PQ and quantification of apoptosis and necrosis cell rates. (E) DHE and MitoSOX staining of human NPCs after 24 h treatment with PQ and quantification of mean DHE and MitoSOX fluorescence intensity. (F) Representative transmission electron microscopy images of human NPCs after 24 h treatment with PQ. Black arrows in low-field images of control cells indicate small vacuoles. Magnified high-field images show normal mitochondria (black arrowheads), swollen mitochondria with disrupted cristae (blue arrowheads), and shrunken mitochondria with ruptured outer membrane (red arrowheads). Scale bars, 5 μm (top panel), 2 μm (bottom panel). (G) Representative flow cytometry graphs of JC-1 staining of human NPCs after 24 h treatment with PQ to evaluate mitochondrial membrane potential and quantification of mean red/green fluorescence intensity ratio. (B, D, E, G) Data are expressed as mean ± SD. (n = 6 independent patient samples), one-way ANOVA, followed by Tukey's multiple comparisons test was used for statistical analysis. (For interpretation of the references to color in this figure legend, the reader is referred to the Web version of this article.)

M, along with histological evidence of degeneration at 18 M, implicates oxidative stress as a potential primary driver of IVD degeneration.

3.5. Search for potential compounds to mitigate the cytotoxicity of mitochondrial superoxide on human NPCs

Based on the above results, we hypothesized that suppression of mitochondrial superoxide could inhibit IVD degeneration. To explore compounds that can mitigate the cytotoxicity of PQ-induced mitochondrial superoxide, human NPCs were pretreated with either NMN, NAC, AA, AA2P, FA, t-FA, or MT for 2 h followed by subjecting cells to PQ for 24 h. The optimal concentration of each compound was determined based on the cell viability assay (Fig. S6). First, exposure to 10 mM PQ reduced cell viability to 66% compared to the control, but all compounds significantly improved it to 84–98%. Exposure to 30 mM PQ reduced cell viability to 35% compared to untreated controls, but only NMN, AA and t-FA were able to significantly limit the viability loss to about 51–54% (Fig. 7A). Therefore, these three compounds were applied in the subsequent experiments. PQ-induced intracellular and mitochondrial superoxide levels were significantly reduced by all three compounds, except with regard to DHE staining in the 30 mM PQ + AA group (Fig. 7B and C).

Next, we investigated whether these compounds could inhibit PQ-induced cellular senescence. All compounds inhibited the increase in SA-β-Gal positivity at 10 mM PQ exposure, but only NMN significantly reduced SA-β-Gal positivity at 30 mM PQ exposure (Fig. 7D). Western blotting showed that activation of the p53-p21 pathway by 10 mM PQ exposure was reduced by all compound treatments, but was irreversible at 30 mM PQ. Conversely, these compound treatments failed to inhibit the activation of the $p16^{INK4a}$ pathway at either concentration (Fig. 7E). Both SOD2 protein expression and SOD activity were further enhanced by NMN treatment under 10 mM PQ exposure, whereas none of the compound treatments were able to rescue the declines caused by 30 mM PQ exposure (Fig. 7E and F). In short, NMN consistently engendered the strongest mitigation of PQ-induced ROS cytotoxicity and cellular senescence in human NPCs and provided significant improvement even at the higher 30 mM PQ dose. This indicates its potential as a promising therapeutic agent against oxidative stress-related disc degeneration and was thus used in subsequent experiments.

3.6. Sod2 deficiency in IVD exacerbates mechanical stress-induced IVD degeneration in a mouse tail-looping model

Mechanical stress, along with aging, stands as a predominant risk factor for IVD degeneration [60,61]. We used a slightly modified tail-looping model to induce IVD degeneration by uneven mechanical loading, as previously reported (Fig. 8A) [44]. The surgery was performed without complications and no evident behavioral changes were observed. This model applies tensile stress on the convex side of the loop and compressive stress on the concave side, enabling the assessment of both mechanical strains on IVD health.

Following successful surgical procedure, we first evaluated whether mechanical overload impacts mitochondrial superoxide levels in IVDs. MitoSOX fluorescence staining in coccygeal IVD of WT mice 24 h after tail-looping surgery showed that mitochondrial superoxide levels increased in both the convex and concave AF regions, with a greater increase on the concave side (Fig. 8B). These findings suggest that compressive stress produces more mitochondrial superoxide than tensile stress.

To evaluate the impact of *Sod2* deficiency on IVD degeneration under mechanical stress and the therapeutic potential of NMN, 15-week-old male WT and *Sod2* cKO mice were injected intraperitoneally with NMN or PBS twice weekly for 4 weeks starting 1 week before tail-looping surgery (Fig. 8C). First, we confirmed that an increase in NAD^+ levels at the presumed site of action was observed over 1–6 h after intraperitoneal injection of NMN in mice and rats (Fig. 8D and Fig. S7A). Tail-looping surgery and NMN administration did not affect the body weight of the mice during the course of the experiments (Fig. S7B). Histology of the control disc at 28 days after tail-looping surgery showed that both WT and *Sod2* cKO mice presented nearly normal morphological features with mild degeneration in the NP region of cKO mice (Figs. S8A and B). In the tail-looped disc, *Sod2* cKO mice exhibited significantly more severe IVD degeneration than WT mice (mean total score; WT: 16.0, cKO: 22.2). Notably, NMN administration effectively attenuated mechanical stress-induced disc degeneration in both WT and *Sod2* cKO mice (Fig. 8E and Fig. S8C). We then defined the convex/concave DHI ratio for radiographic analysis (Fig. 8F). As disc degeneration progresses, disc height on the concave side decreases while disc height on the convex side increases. Consequently, an increase in the convex/concave DHI ratio indicates the progression of disc degeneration. In the control disc, there were no significant changes in DHI over time in any of the groups. In the tail-looped disc, there was no significant difference in the convex/concave DHI ratio among the four groups immediately after surgery, indicating that relatively constant compression could be induced. In the tail-looped disc, *Sod2* cKO mice showed a significant increase in the convex/concave DHI ratio compared to WT mice at 14 days after surgery, and the NMN administration group had a significantly reduced increase in the convex/concave DHI ratio at 28 days after surgery (Fig. 8G and Fig. S7C). We then analyzed nociceptive behavior using the von Frey test. Tail-looping surgery did not significantly change the withdrawal latency of the hind paw and base of the tail. Withdrawal latency in the looped tail decreased in all groups immediately after surgery and showed a tendency to recover over time. However, *Sod2* cKO mice showed a prolonged recovery of withdrawal latency, which was significantly reduced compared to that of WT mice at 28 days after surgery. Furthermore, NMN treatment significantly accelerated the recovery of withdrawal latency, indicating that NMN may have contributed to the pain reduction (Fig. 8H and S Figs. S7D and E).

Finally, we investigated the effects of mechanical overload on SOD2 and COL2 expression in mouse IVD by immunohistochemistry. Interestingly, SOD2 positivity in the tail-looped discs of WT mice was significantly increased in the NP, but decreased in the AF and EP compared to the control disc. Furthermore, SOD2 positivity was significantly decreased on the concave side compared to the convex side in the AF (Fig. 9A and B and Fig. S9). Mitochondrial superoxide levels were markedly elevated on the concave side of the AF compared to the convex side (Fig. 8B), suggesting a potentially greater depletion of SOD2 on the concave side. Notably, NMN administration not only increased SOD2 positivity in the control disc of WT mice, but also increased SOD2

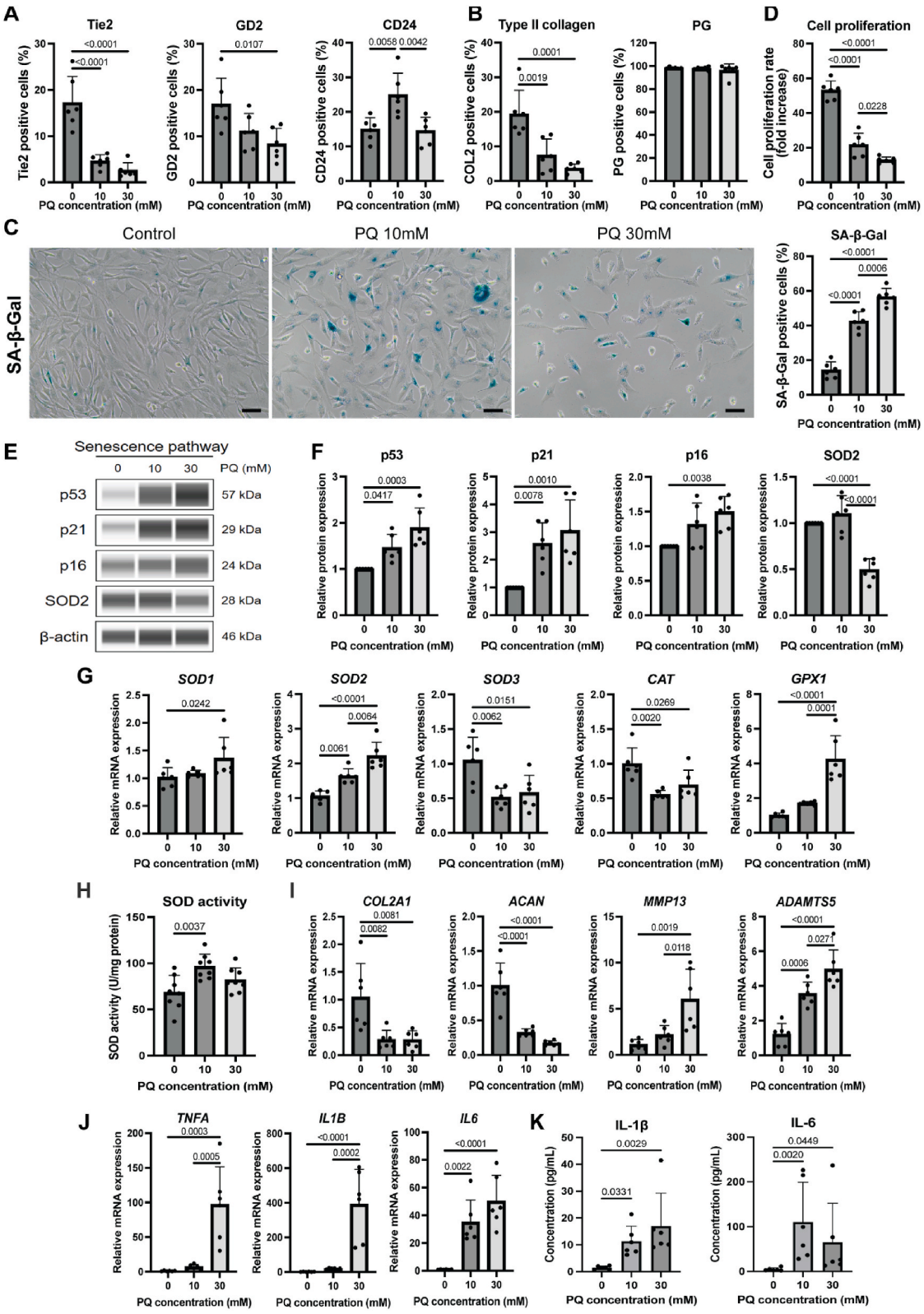

Fig. 4. Excessive mitochondrial superoxide leads to progenitor cell depletion and cellular senescence in human NPCs. (A, B) NPC markers (A) and ECM markers (B) of human NPCs after 48 h treatment with PQ. (C) Representative images of SA-β-Gal staining of human NPCs after 24 h treatment with PQ and quantification of SA-β-Gal positive cell rates. Scale bars, 100 μm. (D) Cell proliferation rate (fold increase) of human NPCs after 48 h treatment with PQ. (E) Western blotting of senescence signaling related p53, p21, $p16^{INK4a}$ and SOD2 in total protein extracts isolated from human NPCs after 24 h treatment with PQ. β-actin was used as a loading control. (F) Quantification of relative protein expression levels. (G) Relative mRNA expression of antioxidant enzymes. (H) SOD activity in total protein extracts isolated from human NPCs after 24 h treatment with PQ. (I–J) Relative mRNA expression of ECM anabolic and catabolic markers (I) and inflammatory cytokines (J) in human NPCs after 48 h treatment with PQ. (K) Secreted catabolic cytokines determined through ELISA. (A-D, F–K) Data are expressed as mean ± SD. (n = 6 independent patient samples), one-way ANOVA, followed by Tukey's multiple comparisons test was used for statistical analysis.

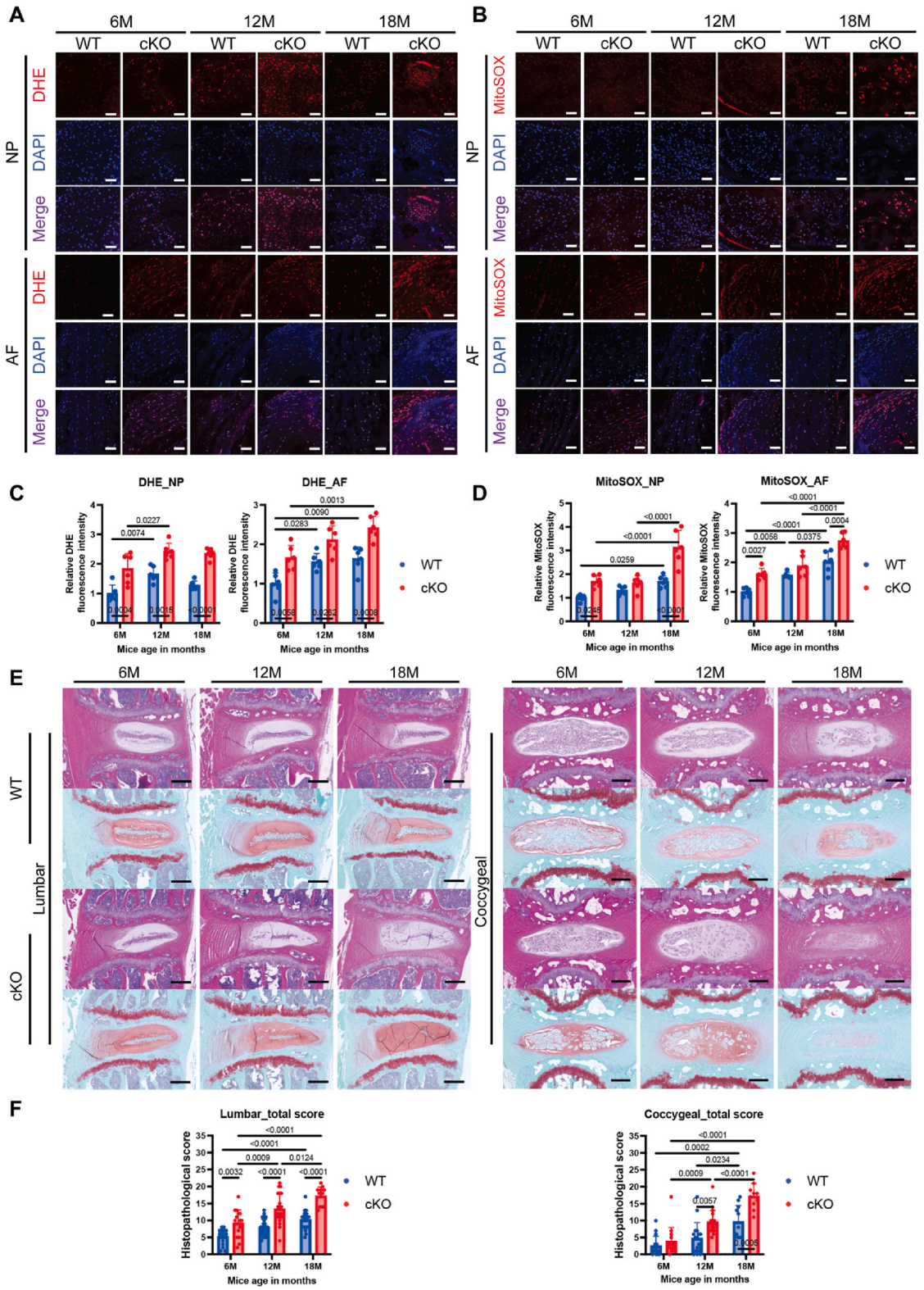

Fig. 5. *Sod2* deficiency in IVD accelerates age-related IVD degeneration in mice. (A, B) Representative images of DHE (A) and MitoSOX (B) fluorescence staining in lumbar IVD of 6 M, 12 M, and 18 M WT and *Sod2* cKO mice. Scale bars, 50 μm. (C, D) Quantification of mean DHE (C) and MitoSOX (D) fluorescence intensity in NP and AF. (E) Representative images of H&E staining (top panel) and safranin-O/fast green staining (bottom panel) in lumbar and coccygeal IVD of 6 M, 12 M, and 18 M WT and *Sod2* cKO mice. Scale bars, 200 μm. (F) Quantification of ORS Spine histopathological score in lumbar and coccygeal IVD. (C, D, F) Data are expressed as mean ± SD. In C, D (n = 6 IVDs from 3 biologically independent mice per group), and F (n = 12–24 IVDs from 6 biologically independent mice per group for lumbar IVD and n = 10–19 IVDs from 6 biologically independent mice per group for coccygeal IVD), two-way ANOVA, followed by Tukey's multiple comparisons test was used for statistical analysis. (For interpretation of the references to color in this figure legend, the reader is referred to the Web version of this article.)

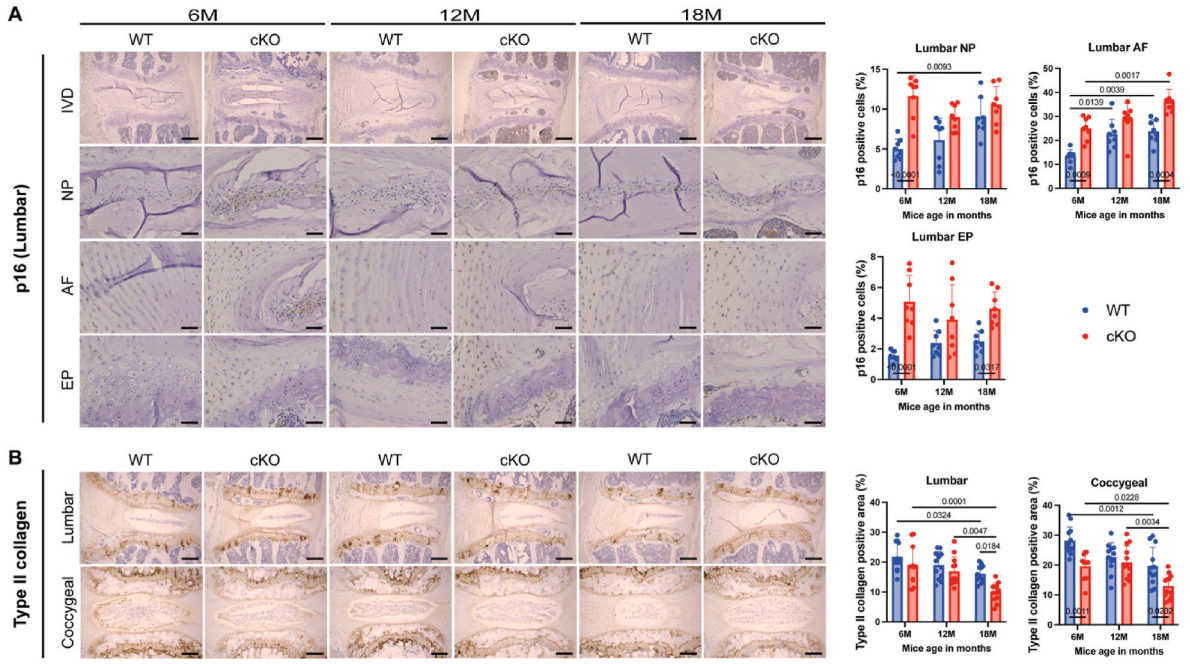

Fig. 6. *Sod2* deficiency in IVD leads to cellular senescence and downregulation of type II collagen expression in mice. (A, B) Representative images of immunohistochemistry of $p16^{INK4a}$ (**A**) and type II collagen (**B**) in lumbar and coccygeal IVD of 6 M, 12 M, and 18 M WT and *Sod2* cKO mice. Right panels show rates of $p16^{INK4a}$-positive cells in NP, AF, and EP and COL2-positive area in NP. Scale bars, 200 μm (IVD in A and B), 50 μm (NP, AF, and EP in A). Data are expressed as mean ± SD. In A (n = 8 IVD from 4 biologically independent mice per group) and in B (n = 12 IVD from 6 biologically independent mice per group), two-way ANOVA, followed by Tukey's multiple comparisons test was used for statistical analysis.

positivity in the tail-looped disc except for the convex side of the AF (Fig. 9A, B and Fig. S9). These results suggest that NMN may have attenuated IVD degeneration by upregulating of SOD2-based protective responses against oxidative stress. In addition, NMN administration rescued the COL2-positivity in tail-looped discs, which was reduced by mechanical overload (Fig. 9C and D). Taken together, these results suggest that *Sod2* deficiency exacerbates mechanical stress-induced IVD degeneration and NMN administration can alleviate disc degeneration by, in part, enhancing SOD2 derived antioxidant activity.

4. Discussion

This study demonstrates that SOD2 plays a pivotal role in maintaining the redox homeostasis in IVDs and that an imbalance between SOD2 and mitochondrial superoxide accelerates IVD degeneration through promoting cellular senescence and ECM degradation (Fig. 9E). In this study, SOD2 expression in the NP of human IVD was upregulated in degenerative discs compared to relatively healthy controls. This is in line with previous single cell RNA sequencing data by Cherif et al. that similarly observed an increase in SOD2 expression as a marker for disc degeneration [62]. Interestingly, our work further suggested that moderate degeneration resulted in an upregulation of SOD2, while severe degeneration did not show a further increase, but rather a decline in SOD activity. Furthermore, the proportion of cells expressing SOD2 showed a strong positive correlation with patient age (Fig. 2). In contrast, SOD2 expression in IVD of WT mice decreased with aging in all three disc-compartments (Fig. S3D and E). Interestingly, under mechanical stress, SOD2 expression exhibited upregulation in the NP and downregulation in the AF and EP (Fig. 9). These results indicate that IVD degeneration is not simply an age-related disease, but is strongly associated with external factors, including mechanical stress. Additionally, the distinct trends in SOD2 expression observed between human and mice discs may be attributed, in part, to the variance in oxygen levels. Furthermore, the rodent NP, which is composed mainly of notochordal cells, and the human NP, which is composed mainly of chondrocyte-like cells, may have different responses to oxidative stress. This may be a topic for future research. The NP is inherently hypoxic [63,64] and is expected to be less exposed to oxidative stress derived from the TCA in its healthy state, thereby potentially maintaining SOD2 expression at low levels in human IVD. In contrast, rodent discs, with their smaller disc volumes and higher oxygen tensions, might experience different redox dynamics [18]. Furthermore, when ROS are induced by external stimuli such as mechanical stress, SOD2 expression in the NP is also enhanced to counteract ROS accumulation. Excessive ROS production can deplete SOD2, resulting in a redox imbalance, that accelerates IVD degeneration. In contrast, the AF and EP maintain high SOD2 expression under healthy conditions, conferring robust antioxidant capabilities. However, upon exposure to ROS induced by aging and mechanical stress, SOD2 expression was found to be compromised.

Emerging evidence suggests that oxidative stress is associated with the development and progression of IVD degeneration [23,24,26]. However, it remained unclear whether oxidative stress directly accelerates IVD degeneration or is merely a consequence of aging. We first demonstrated that superoxide levels in human IVD tissue increases with aging and progressive disc degeneration, along with AGEs, suggesting the accumulation of oxidative damage (Fig. 2). Notably, both aging and mechanical stress, which are the two major risk factors for IVD degeneration [16,61], elevated superoxide levels in the IVD of WT mice (Figs. 5 and 8). Furthermore, the finding that elevated superoxide in the IVD (observed in 12 M WT mice) precedes histologically evident disc degeneration (observed in 18 M WT mice) suggests that oxidative stress plays a critical role in the onset and progression of disc degeneration (Fig. 5). In addition, we found that superoxide levels were consistently elevated in *Sod2* cKO mice compared to WT mice at all ages and that *Sod2* deficiency in IVD accelerates age-related disc degeneration and exacerbates mechanical stress-induced disc degeneration in mice (Figs. 5 and 8). Taken together, these findings support the suggestion that SOD2 plays an essential role in limiting disc degeneration by maintaining redox homeostasis in IVD.

Several studies have suggested that cellular senescence is an

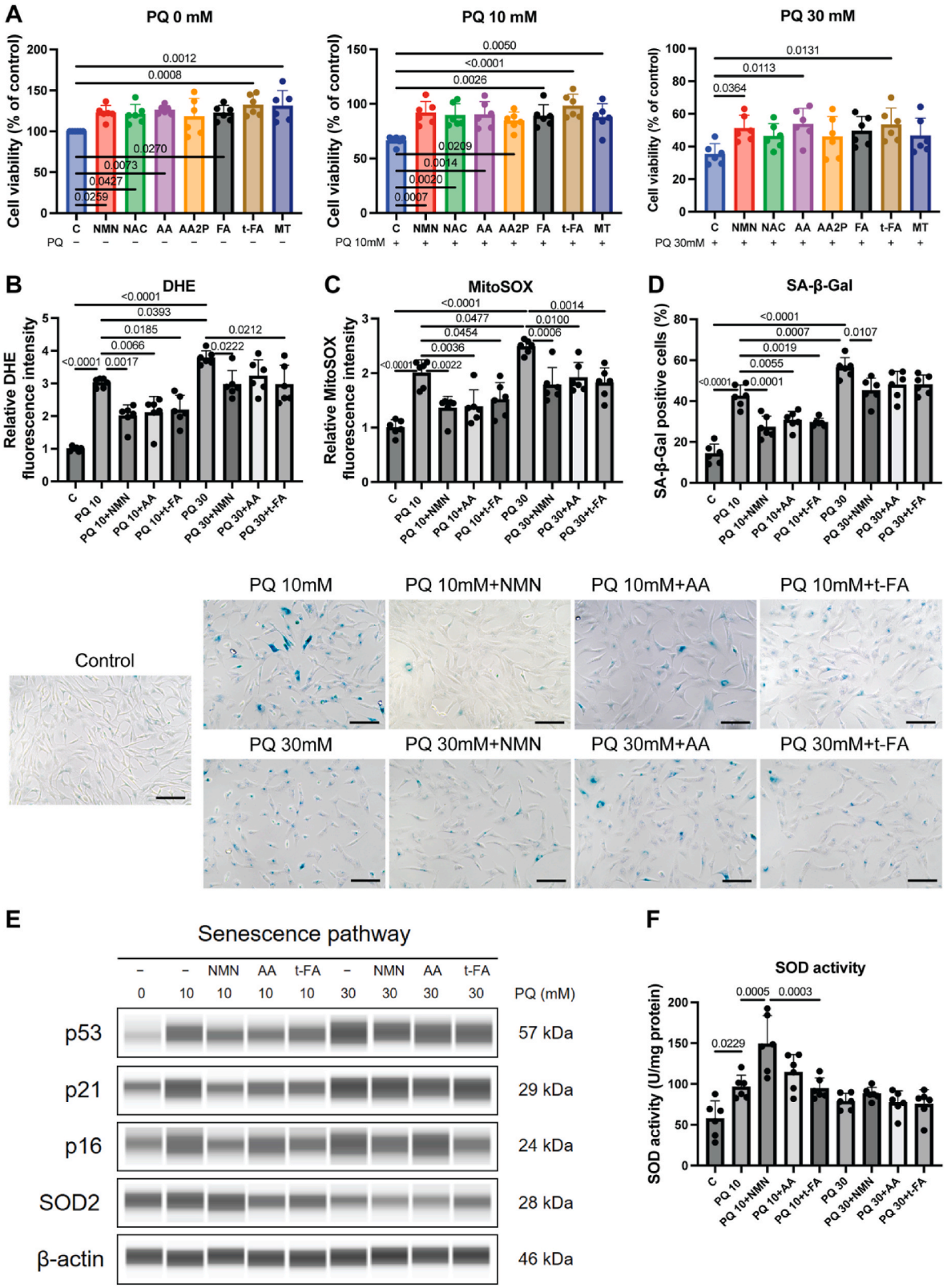

Fig. 7. Search for potential compounds to mitigate the cytotoxicity of mitochondrial superoxide on human NPCs. (A) Cell viability of human NPCs after 24 h treatment with PQ following 2 h pretreatment with/without either β-nicotinamide mononucleotide (NMN), N-acetylcysteine (NAC), L-ascorbic acid (AA), L-ascorbic acid 2-phosphate sesquimagnesium salt hydrate (AA2P), ferulic acid (FA), *trans*-ferulic acid (t-FA), or MitoTEMPO (MT). (B, C) DHE (B) and MitoSOX (C) staining of human NPCs after 24 h treatment with PQ following 2 h pretreatment with either NMN, AA, or t-FA and quantification of mean DHE and MitoSOX fluorescence intensity. (D) Representative images of SA-β-Gal staining of human NPCs after the same treatment as above and quantification of SA-β-Gal positive cell rates. Scale bars, 100 μm. (E) Western blotting of senescence signaling related p53, p21, $p16^{INK4a}$ and SOD2 in total protein extracts isolated from human NPCs after the same treatment as above. (F) SOD activity in total protein extracts isolated from human NPCs after the same treatment as above. (A-D, F) Data are expressed as mean ± SD. (n = 6 independent patient samples), one-way ANOVA, followed by Tukey's multiple comparisons test was used for statistical analysis.

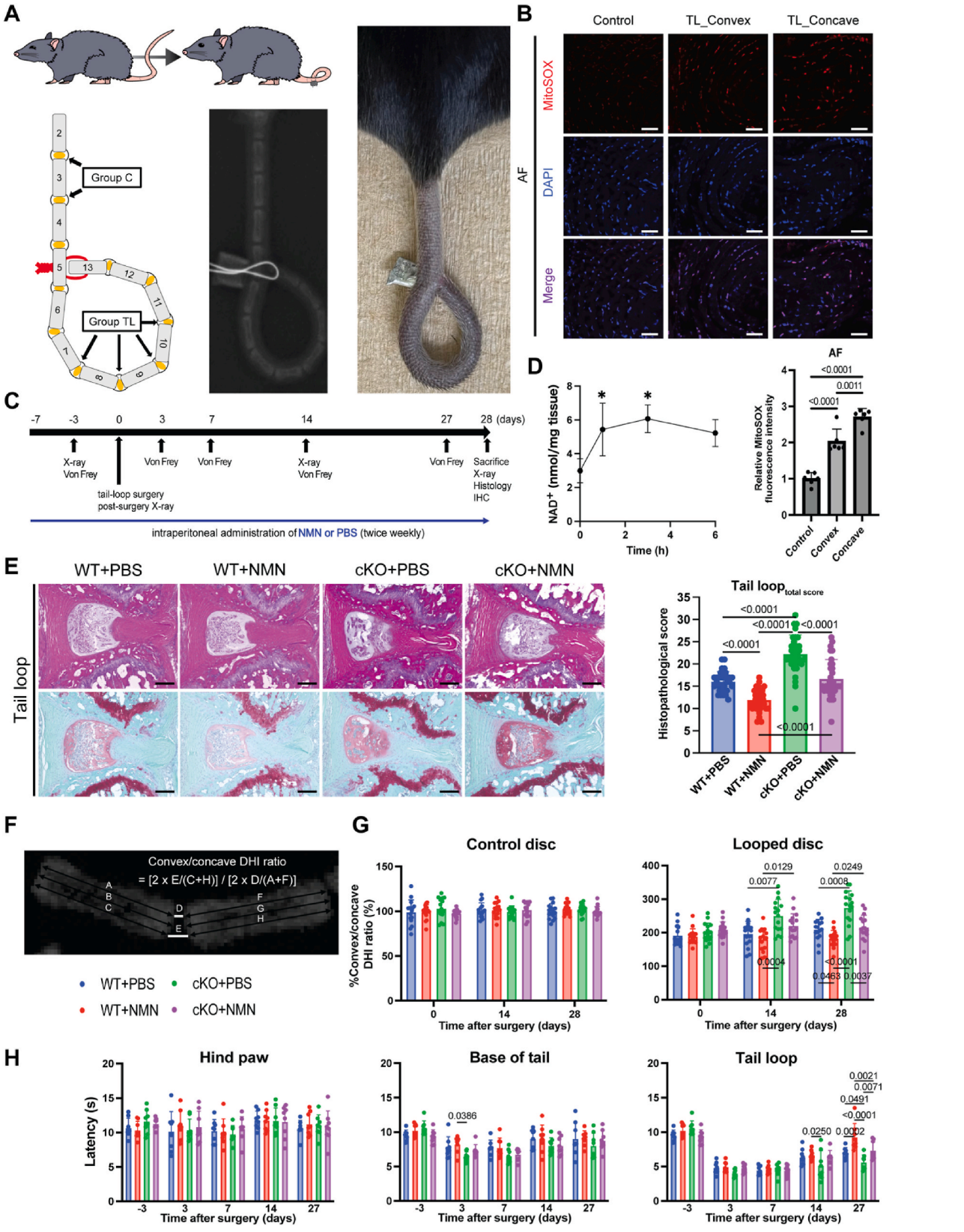

(caption on next page)

Fig. 8. *Sod2* deficiency in IVD exacerbates mechanical stress-induced IVD degeneration in a mouse tail-looping model. (A) Schematic illustration, radiograph, and picture of the tail-looping model. (B) Representative images of MitoSOX fluorescence staining in coccygeal IVD of 15-week-old male WT mice 24 h after tail-looping surgery and quantification of mean MitoSOX fluorescence intensity in AF. Scale bars, 50 μm. (C) Schematic illustration of the experimental design in NMN-treated mouse tail-looping model. (D) Temporal assessment of NAD^+ conversion in spinal unit following NMN treatment. (E) Representative images of H&E staining and safranin-O/fast green staining in coccygeal IVD of WT and *Sod2* cKO mice 28 days after tail-looping surgery and quantification of ORS Spine histopathological score. Scale bars, 200 μm. (F) A visual representation of the disc height index (DHI) measurement. (G) Changes in the %convex/concave DHI ratio of control and tail-looped discs. (H) Withdrawal latency times in the von Frey test. (B, D, E, G, H) Data are expressed as mean ± SD. In B (n = 6 IVDs from 3 biologically independent mice per group), D (n = 3 biologically independent mice per group), E (n = 32 IVDs from 8 biologically independent mice per group), G (n = 16 IVDs from 8 biologically independent mice per group), and H (n = 8 biologically independent mice per group), one-way ANOVA for B and E, two-way ANOVA for G and H followed by Tukey's multiple comparison test were used for statistical analysis. One-way ANOVA for D followed by Dunnett's multiple comparisons test was used for statistical analysis. * indicates $p < 0.05$. (For interpretation of the references to color in this figure legend, the reader is referred to the Web version of this article.)

important contributor to the progression of IVD degeneration [65–68]. Senescent cells are generally characterized by growth arrest, resistance to apoptosis, and an altered gene expression, including upregulation of cell cycle inhibitors such as $p16^{INK4a}$, p53, and p21, as well as secretion of various bioactive molecules, leading to the SASP [56,57]. Cellular senescence can be triggered by a variety of intrinsic and extrinsic stimuli, including telomere shortening, DNA damage, oncogenes, and various forms of stress, including oxidative, endoplasmic reticulum, and mitotic stress [56,57]. In this study, we examined the effects of PQ-induced mitochondrial superoxide on the phenotype and cellular senescence of human NPCs to investigate the relationship between oxidative stress and cellular senescence in the IVD. We demonstrated that excessive mitochondrial superoxide leads to mitochondrial dysfunction, progenitor cell depletion, cellular senescence and subsequent upregulation of SASP factors associated with ECM degradation in human NPCs (Figs. 3 and 4). Furthermore, $p16^{INK4a}$ positivity in IVD of WT mice increased slightly with age, while *Sod2* deficiency resulted in significantly higher $p16^{INK4a}$ positivity even in young mice at 6 M of age. Moreover, *Sod2* deficiency resulted in a marked reduction in COL2 expression in IVD (Fig. 6 and Fig. S5). These results suggest that an imbalance between SOD2 and mitochondrial superoxide accelerates cellular senescence and ECM degradation in IVD.

In recent years, the therapeutic potential of various antioxidants targeting oxidative stress against IVD degeneration has been reported [26,69]; however, the optimal compounds have not been identified. Therefore, we investigated an array of antioxidant compounds that could potentially mitigate the cytotoxicity of PQ-induced mitochondrial superoxide on human NPCs. Interestingly, our results indicate that NMN outperformed conventional antioxidants, namely NAC and AA, in preserving cell viability and attenuating cellular senescence against PQ-induced mitochondrial superoxide. NMN is a critical precursor molecule of nicotinamide adenine dinucleotide (NAD^+), a key player in the energy metabolism. More specifically, NAD is a regulator of NAD-dependent enzymes sirtuins, which through deacetylation, are able to activate SOD activity, including SOD2 [70]. Thus, NMN may have mediated these cytoprotective responses by augmenting SOD activity and enhancing antioxidant capacities (Fig. 7). Moreover, our results affirmed NMN's ability to directly boost NAD^+ levels within the spinal units of mouse discs (Fig. 8D), a finding further supported in rat discs (Fig. S7A). This underscores the NMN's potential to impart antioxidative effects even in the avascular disc environment. It's noteworthy that the validation in a rat model was necessitated by challenges in acquiring a sufficient amount of mouse disc material; hence, the entire spinal unit was examined for mouse samples. A previous study showed that NMN could restore mitochondrial antioxidants and reduce apoptosis in human NPCs against AGEs-induced IVD degeneration through adenosine monophosphate-activated protein kinase and peroxisome proliferator-activated receptor-γ coactivator 1α (AMPK-PGC-1α) pathway [71]. Additionally, our results imply the existence of a therapeutic efficacy threshold for these compounds targeting mitochondrial superoxide; they may be beneficial for moderate IVD degeneration but potentially insufficient to mitigate severe stress-induced degeneration. We further demonstrated that NMN administration attenuated mechanical stress-induced IVD degeneration in a mouse tail-looping model, as evidenced by histological, radiographic, and nociceptive assessments (Fig. 8). However, considering that NMN was also able to alleviate the progression of disc degeneration in *Sod2* cKO mice, it underscores that its mechanism is not limited to regulating SOD2 activity. Collectively, our findings suggest that mitochondrial superoxide may represent a promising novel therapeutic target for IVD degeneration.

This study has several limitations. First, only human NP tissues and cells were evaluated due to the difficulty in obtaining AF and EP tissues by nucleotomy, where NP is resected for curative purposes. Second, the IVD of mouse is biologically and mechanically different from that of humans. Specifically, rodents retain notochordal cells in the NP throughout life, resulting in less age-related disc pathology [72]. Moreover, our results suggest a distinct SOD2 expression pattern with age and degeneration that requires consideration when translating the mice observation to the human condition. Additionally, our surgical tail-looping mouse model to induce IVD degeneration does not fully mimic the clinical situation of human degenerative discs. Acknowledging the limitations, the mouse model, with its utility and genetic manipulability [73] and similar disc geometry [74], provides valuable insights into IVD degeneration despite inherent differences from the human condition [18,46,72]. Future preclinical studies could be performed using larger animal models in which the notochordal cells in the NP disappear. In addition, the *Sod2* cKO model used in this study selectively eliminates SOD2 from all chondrogenic cells expressing *Col2a1*. It's important to note that other cartilage tissues beyond the IVD were not specifically investigated in this study. Nonetheless, our previous work using this mouse model has confirmed that the potential impact on overall health is not significantly different compared to control mice [34]. Finally, the therapeutic potential of antioxidants for age-related IVD degeneration was not evaluated and warrants future study.

In conclusion, our study sheds light on the critical role of SOD2 in preserving redox homeostasis within IVD. The imbalance between SOD2 and mitochondrial superoxide can induce and accelerate IVD degeneration in part through promoting cellular senescence and ECM degradation. These findings mark a significant advancement in unraveling the complexities of IVD degeneration, contributing valuable insights with broader implications for oxidative stress-related pathologies.

Data availability

All data needed to evaluate the conclusions in the paper are present in the paper and/or the Supplementary Materials. All raw data and statistical p-values are provided in the source data file. Additional data related to this paper may be requested from the authors.

CRediT authorship contribution statement

Shota Tamagawa: Conceptualization, Data curation, Formal analysis, Investigation, Methodology, Project administration, Resources, Software, Visualization, Writing – original draft. **Daisuke Sakai:** Conceptualization, Funding acquisition, Methodology, Project administration, Resources, Supervision, Validation, Writing – review & editing. **Hidetoshi Nojiri:** Methodology, Supervision, Validation, Writing –

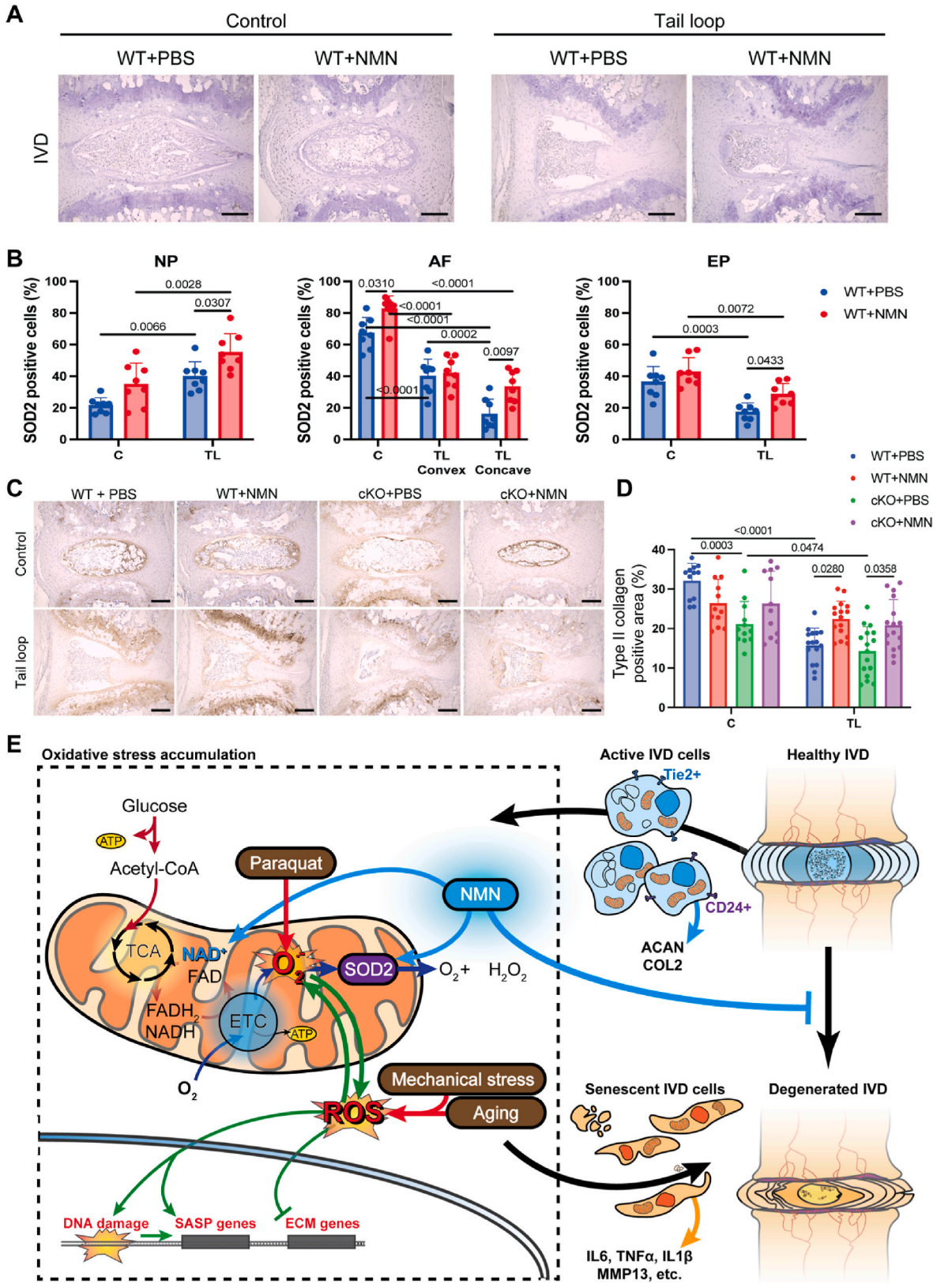

Fig. 9. Effects of mechanical overload on SOD2 and COL2 expression in mouse IVD. (A) Representative images of immunohistochemistry of SOD2 in coccygeal IVD of WT mice 28 days after tail-looping surgery. Scale bars, 200 μm (IVD), 50 μm (NP, AF, and EP). (B) Comparison of SOD2-positive cell rates in control and tail-looped disc from WT mice with and without NMN administration. (C) Representative images of immunohistochemistry of COL2 in coccygeal IVD of WT and *Sod2* cKO mice 28 days after tail-looping surgery. Scale bars, 200 μm. (D) Quantification of COL2-positive area in NP. **e** Schematic diagram representing the potential mechanism by which SOD2 regulates redox homeostasis of the IVD during aging and mechanical stress. (B, D) Data are expressed as mean ± SD. In B (n = 8 IVDs from 4 biologically independent mice per group) and D (n = 12 IVDs for control and n = 16 IVDs for tail loop from 8 biologically independent mice per group), two-way ANOVA followed by Tukey's multiple comparison test was used for statistical analysis.

review & editing. **Yoshihiko Nakamura:** Data curation, Formal analysis, Methodology, Writing – review & editing. **Takayuki Warita:** Data curation, Formal analysis, Investigation, Methodology, Validation, Writing – review & editing. **Erika Matsushita:** Data curation, Formal analysis, Methodology, Writing – review & editing. **Jordy Schol:** Data curation, Methodology, Validation, Visualization, Writing – original draft, Writing – review & editing. **Hazuki Soma:** Data curation, Investigation, Writing – review & editing. **Shota Ogasawara:** Data curation, Formal analysis, Investigation, Writing – review & editing. **Daiki Munesada:** Data curation, Formal analysis, Investigation, Writing – review & editing. **Masato Koike:** Methodology, Supervision, Validation, Writing – review & editing. **Takahiko Shimizu:** Methodology, Resources, Supervision, Validation, Writing – review & editing. **Masato Sato:** Supervision, Writing – review & editing. **Muneaki Ishijima:** Supervision, Writing – review & editing. **Masahiko Watanabe:** Supervision, Writing – review & editing.

Declaration of competing interest

The authors declare that they have no known competing financial interests or personal relationships that could have appeared to influence the work reported in this paper.

Acknowledgments

The authors thank the Medical Science College Office, Tokai University, for technical assistance. This work was supported by JSPS KAKENHI Grant Number JP20H03809 (D.S.).

Appendix A. Supplementary data

Supplementary data to this article can be found online at https://doi.org/10.1016/j.redox.2024.103091.

References

[1] D. Hoy, L. March, P. Brooks, F. Blyth, A. Woolf, C. Bain, G. Williams, E. Smith, T. Vos, J. Barendregt, et al., The global burden of low back pain: estimates from the Global Burden of Disease 2010 study, Ann. Rheum. Dis. 73 (2014) 968–974, https://doi.org/10.1136/annrheumdis-2013-204428.

[2] J. Hartvigsen, M.J. Hancock, A. Kongsted, Q. Louw, M.L. Ferreira, S. Genevay, D. Hoy, J. Karppinen, G. Pransky, J. Sieper, et al., What low back pain is and why we need to pay attention, Lancet (London, England) 391 (2018) 2356–2367, https://doi.org/10.1016/S0140-6736(18)30480-X.

[3] Global burden of 369 diseases and injuries in 204 countries and territories, 1990-2019: a systematic analysis for the Global Burden of Disease Study 2019, Lancet 396 (2020) 1204–1222, https://doi.org/10.1016/s0140-6736(20)30925-9.

[4] N.N. Knezevic, K.D. Candido, J.W.S. Vlaeyen, J. Van Zundert, S.P. Cohen, Low back pain, Lancet 398 (2021) 78–92, https://doi.org/10.1016/s0140-6736(21)00733-9.

[5] G. Livshits, M. Popham, I. Malkin, P.N. Sambrook, A.J. Macgregor, T. Spector, F. M. Williams, Lumbar disc degeneration and genetic factors are the main risk factors for low back pain in women: the UK Twin Spine Study, Ann. Rheum. Dis. 70 (2011) 1740–1745, https://doi.org/10.1136/ard.2010.137836.

[6] S. Tamagawa, D. Sakai, H. Nojiri, M. Sato, M. Ishijima, M. Watanabe, Imaging evaluation of intervertebral disc degeneration and painful discs—advances and challenges in quantitative MRI, Diagnostics 12 (2022) 707.

[7] N. Boos, S. Weissbach, H. Rohrbach, C. Weiler, K.F. Spratt, A.G. Nerlich, Classification of age-related changes in lumbar intervertebral discs: 2002 Volvo Award in basic science, Spine 27 (2002) 2631–2644, https://doi.org/10.1097/00007632-200212010-00002 (Phila Pa 1976).

[8] M.A. Adams, P.J. Roughley, What is intervertebral disc degeneration, and what causes it? Spine 31 (2006) 2151–2161, https://doi.org/10.1097/01.brs.0000231761.73859.2c.

[9] A.L.A. Binch, J.C. Fitzgerald, E.A. Growney, F. Barry, Cell-based strategies for IVD repair: clinical progress and translational obstacles, Nat. Rev. Rheumatol. 17 (2021) 158–175, https://doi.org/10.1038/s41584-020-00568-w.

[10] D. Sakai, J. Schol, M. Watanabe, Clinical development of regenerative medicine targeted for intervertebral disc disease, Medicina (Kaunas) 58 (2022), https://doi.org/10.3390/medicina58020267.

[11] J.P. Urban, S. Roberts, Degeneration of the intervertebral disc, Arthritis Res. Ther. 5 (2003) 120–130, https://doi.org/10.1186/ar629.

[12] J.P. Urban, S. Smith, J.C. Fairbank, Nutrition of the intervertebral disc, Spine 29 (2004) 2700–2709, https://doi.org/10.1097/01.brs.0000146499.97948.52 (Phila Pa 1976).

[13] D.E. Fournier, P.K. Kiser, J.K. Shoemaker, M.C. Battié, C.A. Séguin, Vascularization of the human intervertebral disc: a scoping review, JOR Spine 3 (2020) e1123, https://doi.org/10.1002/jsp2.1123.

[14] P.P.A. Vergroesen, I. Kingma, K.S. Emanuel, R.J.W. Hoogendoorn, T.J. Welting, B. J. van Royen, J.H. van Dieën, T.H. Smit, Mechanics and biology in intervertebral disc degeneration: a vicious circle, Osteoarthritis Cartilage 23 (2015) 1057–1070, https://doi.org/10.1016/j.joca.2015.03.028.

[15] M.V. Risbud, I.M. Shapiro, Role of cytokines in intervertebral disc degeneration: pain and disc content, Nat. Rev. Rheumatol. 10 (2014) 44–56, https://doi.org/10.1038/nrrheum.2013.160.

[16] N.V. Vo, R.A. Hartman, P.R. Patil, M.V. Risbud, D. Kletsas, J.C. Iatridis, J. A. Hoyland, C.L. Le Maitre, G.A. Sowa, J.D. Kang, Molecular mechanisms of biological aging in intervertebral discs, J. Orthop. Res. 34 (2016) 1289–1306, https://doi.org/10.1002/jor.23195.

[17] X. Yin, A. Motorwala, O. Vesvoranan, H.B. Levene, W. Gu, C.-Y. Huang, Effects of glucose deprivation on ATP and proteoglycan production of intervertebral disc cells under hypoxia, Sci. Rep. 10 (2020) 8899, https://doi.org/10.1038/s41598-020-65691-w.

[18] E.E. McDonnell, N. Wilson, M.N. Barcellona, T. Ní Néill, J. Bagnall, P.A.J. Brama, G.M. Cunniffe, S.L. Darwish, J.S. Butler, C.T. Buckley, Preclinical to clinical translation for intervertebral disc repair: effects of species-specific scale, metabolism, and matrix synthesis rates on cell-based regeneration, JOR SPINE 6 (2023) e1279, https://doi.org/10.1002/jsp2.1279.

[19] C.-Y.C. Huang, T.-Y. Yuan, A.R. Jackson, L. Hazbun, C. Fraker, W.Y. Gu, Effects of low glucose concentrations on oxygen consumption rates of intervertebral disc cells, Spine 32 (2007) 2063–2069, https://doi.org/10.1097/BRS.0b013e318145a521.

[20] Y. Song, S. Lu, W. Geng, X. Feng, R. Luo, G. Li, C. Yang, Mitochondrial quality control in intervertebral disc degeneration, Exp. Mol. Med. 53 (2021) 1124–1133, https://doi.org/10.1038/s12276-021-00650-7.

[21] E.S. Silagi, E. Schipani, I.M. Shapiro, M.V. Risbud, The role of HIF proteins in maintaining the metabolic health of the intervertebral disc, Nat. Rev. Rheumatol. 17 (2021) 426–439, https://doi.org/10.1038/s41584-021-00621-2.

[22] S. Holm, A. Maroudas, J.P. Urban, G. Selstam, A. Nachemson, Nutrition of the intervertebral disc: solute transport and metabolism, Connect. Tissue Res. 8 (1981) 101–119, https://doi.org/10.3109/03008208109152130.

[23] A. Dimozi, E. Mavrogonatou, A. Sklirou, D. Kletsas, Oxidative stress inhibits the proliferation, induces premature senescence and promotes a catabolic phenotype in human nucleus pulposus intervertebral disc cells, Eur. Cell. Mater. 30 (2015) 89–102, https://doi.org/10.22203/ecm.v030a07. ; discussion 103.

[24] S. Suzuki, N. Fujita, N. Hosogane, K. Watanabe, K. Ishii, Y. Toyama, K. Takubo, K. Horiuchi, T. Miyamoto, M. Nakamura, et al., Excessive reactive oxygen species are therapeutic targets for intervertebral disc degeneration, Arthritis Res. Ther. 17 (2015) 316, https://doi.org/10.1186/s13075-015-0834-8.

[25] F. Wang, F. Cai, R. Shi, X.H. Wang, X.T. Wu, Aging and age related stresses: a senescence mechanism of intervertebral disc degeneration, Osteoarthritis Cartilage 24 (2016) 398–408, https://doi.org/10.1016/j.joca.2015.09.019.

[26] C. Feng, M. Yang, M. Lan, C. Liu, Y. Zhang, B. Huang, H. Liu, Y.R.O.S. Zhou, Crucial intermediators in the pathogenesis of intervertebral disc degeneration, Oxid. Med. Cell. Longev. 2017 (2017) 5601593, https://doi.org/10.1155/2017/5601593.

[27] I. Fridovich, Superoxide radical and superoxide dismutases, Annu. Rev. Biochem. 64 (1995) 97–112, https://doi.org/10.1146/annurev.bi.64.070195.000525.

[28] T. Finkel, N.J. Holbrook, Oxidants, oxidative stress and the biology of ageing, Nature 408 (2000) 239–247, https://doi.org/10.1038/35041687.

[29] J.E. Kokoszka, P. Coskun, L.A. Esposito, D.C. Wallace, Increased mitochondrial oxidative stress in the Sod2 (+/-) mouse results in the age-related decline of mitochondrial function culminating in increased apoptosis, Proc. Natl. Acad. Sci. U.S.A. 98 (2001) 2278–2283, https://doi.org/10.1073/pnas.051627098.

[30] H. Nojiri, T. Shimizu, M. Funakoshi, O. Yamaguchi, H. Zhou, S. Kawakami, Y. Ohta, M. Sami, T. Tachibana, H. Ishikawa, et al., Oxidative stress causes heart failure with impaired mitochondrial respiration, J. Biol. Chem. 281 (2006) 33789–33801, https://doi.org/10.1074/jbc.M602118200.

[31] L. Esposito, J. Raber, L. Kekonius, F. Yan, G.Q. Yu, N. Bien-Ly, J. Puoliväli, K. Scearce-Levie, E. Masliah, L. Mucke, Reduction in mitochondrial superoxide dismutase modulates Alzheimer's disease-like pathology and accelerates the onset of behavioral changes in human amyloid precursor protein transgenic mice, J. Neurosci. 26 (2006) 5167–5179, https://doi.org/10.1523/JNEUROSCI.0482-06.2006.

[32] L. Miao, D.K. St Clair, Regulation of superoxide dismutase genes: implications in disease, Free Radic. Biol. Med. 47 (2009) 344–356, https://doi.org/10.1016/j.freeradbiomed.2009.05.018.

[33] S.L. Archer, G. Marsboom, G.H. Kim, H.J. Zhang, P.T. Toth, E.C. Svensson, J.R. B. Dyck, M. Gomberg-Maitland, B. Thébaud, A.N. Husain, et al., Epigenetic attenuation of mitochondrial superoxide dismutase 2 in pulmonary arterial hypertension: a basis for excessive cell proliferation and a new therapeutic target, Circulation 121 (2010) 2661–2671, https://doi.org/10.1161/CIRCULATIONAHA.109.916098.

[34] M. Koike, H. Nojiri, Y. Ozawa, K. Watanabe, Y. Muramatsu, H. Kaneko, D. Morikawa, K. Kobayashi, Y. Saita, T. Sasho, et al., Mechanical overloading causes mitochondrial superoxide and SOD2 imbalance in chondrocytes resulting in cartilage degeneration, Sci. Rep. 5 (2015) 11722, https://doi.org/10.1038/srep11722.

[35] Shalash, W.; Ahrens, S.R.; Bardonova, L.A.; Byvaltsev, V.A.; Giers, M.B. Patient-specific apparent diffusion maps used to model nutrient availability in degenerated intervertebral discs. JOR SPINE n/a, e1179, doi:https://doi.org/10.1002/jsp2.1179.

[36] K. Sako, D. Sakai, Y. Nakamura, J. Schol, E. Matsushita, T. Warita, N. Horikita, M. Sato, M. Watanabe, Effect of whole tissue culture and basic fibroblast growth factor on maintenance of Tie2 molecule expression in human nucleus pulposus cells, Int. J. Mol. Sci. (2021) 22, https://doi.org/10.3390/ijms22094723.
[37] S. Tamagawa, D. Sakai, J. Schol, K. Sako, Y. Nakamura, E. Matsushita, T. Warita, S. Hazuki, H. Nojiri, M. Sato, et al., N-acetylcysteine attenuates oxidative stress-mediated cell viability loss induced by dimethyl sulfoxide in cryopreservation of human nucleus pulposus cells: a potential solution for mass production, JOR Spine 5 (2022) e1223, https://doi.org/10.1002/jsp2.1223.
[38] F. Mwale, I. Ciobanu, D. Giannitsios, P. Roughley, T. Steffen, J. Antoniou, Effect of oxygen levels on proteoglycan synthesis by intervertebral disc cells, Spine 36 (2011) E131–E138, https://doi.org/10.1097/BRS.0b013e3181d52b9e (Phila Pa 1976).
[39] H.M. Cochemé, M.P. Murphy, Complex I is the major site of mitochondrial superoxide production by paraquat, J. Biol. Chem. 283 (2008) 1786–1798, https://doi.org/10.1074/jbc.M708597200.
[40] T. Blanco-Ayala, A.C. Andérica-Romero, J. Pedraza-Chaverri, New insights into antioxidant strategies against paraquat toxicity, Free Radic. Res. 48 (2014) 623–640, https://doi.org/10.3109/10715762.2014.899694.
[41] D.A. Ovchinnikov, J.M. Deng, G. Ogunrinu, R.R. Behringer, Col2a1-directed expression of Cre recombinase in differentiating chondrocytes in transgenic mice, Genesis 26 (2000) 145–146.
[42] T. Ikegami, Y. Suzuki, T. Shimizu, K. Isono, H. Koseki, T. Shirasawa, Model mice for tissue-specific deletion of the manganese superoxide dismutase (MnSOD) gene, Biochem. Biophys. Res. Commun. 296 (2002) 729–736, https://doi.org/10.1016/s0006-291x(02)00933-6.
[43] T. Ohnishi, H. Sudo, T. Tsujimoto, N. Iwasaki, Age-related spontaneous lumbar intervertebral disc degeneration in a mouse model, J. Orthop. Res. 36 (2018) 224–232, https://doi.org/10.1002/jor.23634.
[44] D. Sakai, K. Nishimura, M. Tanaka, D. Nakajima, S. Grad, M. Alini, H. Kawada, K. Ando, J. Mochida, Migration of bone marrow-derived cells for endogenous repair in a new tail-looping disc degeneration model in the mouse: a pilot study, Spine J. 15 (2015) 1356–1365, https://doi.org/10.1016/j.spinee.2013.07.491.
[45] A.P. Gomes, N.L. Price, A.J. Ling, J.J. Moslehi, M.K. Montgomery, L. Rajman, J. P. White, J.S. Teodoro, C.D. Wrann, B.P. Hubbard, et al., Declining NAD(+) induces a pseudohypoxic state disrupting nuclear-mitochondrial communication during aging, Cell 155 (2013) 1624–1638, https://doi.org/10.1016/j.cell.2013.11.037.
[46] I.P. Melgoza, S.S. Chenna, S. Tessier, Y. Zhang, S.Y. Tang, T. Ohnishi, E.J. Novais, G.J. Kerr, S. Mohanty, V. Tam, et al., Development of a standardized histopathology scoring system using machine learning algorithms for intervertebral disc degeneration in the mouse model-An ORS spine section initiative, JOR Spine 4 (2021) e1164, https://doi.org/10.1002/jsp2.1164.
[47] A.R. Crowe, W. Yue, Semi-quantitative determination of protein expression using immunohistochemistry staining and analysis: an integrated protocol, Bio Protoc 9 (2019), https://doi.org/10.21769/BioProtoc.3465.
[48] D. Sakai, J. Schol, F.C. Bach, A. Tekari, N. Sagawa, Y. Nakamura, S.C.W. Chan, T. Nakai, L.B. Creemers, D.A. Frauchiger, et al., Successful fishing for nucleus pulposus progenitor cells of the intervertebral disc across species, JOR SPINE 1 (2018) e1018, https://doi.org/10.1002/jsp2.1018.
[49] K. Masuda, Y. Aota, C. Muehleman, Y. Imai, M. Okuma, E.J. Thonar, G. B. Andersson, H.S. An, A novel rabbit model of mild, reproducible disc degeneration by an anulus needle puncture: correlation between the degree of disc injury and radiological and histological appearances of disc degeneration, Spine 30 (2005) 5–14, https://doi.org/10.1097/01.brs.0000148152.04401.20 (Phila Pa 1976).
[50] K. Ura, K. Yamada, T. Tsujimoto, D. Ukeba, N. Iwasaki, H. Sudo, Ultra-purified alginate gel implantation decreases inflammatory cytokine levels, prevents intervertebral disc degeneration, and reduces acute pain after discectomy, Sci. Rep. 11 (2021) 638, https://doi.org/10.1038/s41598-020-79958-9.
[51] G. Vistoli, D. De Maddis, A. Cipak, N. Zarkovic, M. Carini, G. Aldini, Advanced glycoxidation and lipoxidation end products (AGEs and ALEs): an overview of their mechanisms of formation, Free Radic. Res. 47 (2013) 3–27, https://doi.org/10.3109/10715762.2013.815348.
[52] F. Yamakura, H. Kawasaki, Post-translational modifications of superoxide dismutase, Biochim. Biophys. Acta 1804 (2010) 318–325, https://doi.org/10.1016/j.bbapap.2009.10.010.
[53] R.J. Williams, L.T. Laagland, F.C. Bach, L. Ward, W. Chan, V. Tam, A. Medzikovic, S. Basatvat, L. Paillat, N. Vedrenne, et al., Recommendations for intervertebral disc notochordal cell investigation: from isolation to characterization, JOR SPINE 6 (2023) e1272, https://doi.org/10.1002/jsp2.1272.
[54] D. Sakai, Y. Nakamura, T. Nakai, T. Mishima, S. Kato, S. Grad, M. Alini, M. V. Risbud, D. Chan, K.S. Cheah, et al., Exhaustion of nucleus pulposus progenitor cells with ageing and degeneration of the intervertebral disc, Nat. Commun. 3 (2012) 1264, https://doi.org/10.1038/ncomms2226.
[55] M.V. Risbud, Z.R. Schoepflin, F. Mwale, R.A. Kandel, S. Grad, J.C. Iatridis, D. Sakai, J.A. Hoyland, Defining the phenotype of young healthy nucleus pulposus cells: recommendations of the Spine Research Interest Group at the 2014 annual ORS meeting, J. Orthop. Res. 33 (2015) 283–293, https://doi.org/10.1002/jor.22789.
[56] D. Muñoz-Espín, M. Serrano, Cellular senescence: from physiology to pathology, Nat. Rev. Mol. Cell Biol. 15 (2014) 482–496, https://doi.org/10.1038/nrm3823.
[57] J.M. van Deursen, The role of senescent cells in ageing, Nature 509 (2014) 439–446, https://doi.org/10.1038/nature13193.
[58] J.-P. Coppé, C.K. Patil, F. Rodier, Y. Sun, D.P. Muñoz, J. Goldstein, P.S. Nelson, P.-Y. Desprez, J. Campisi, Senescence-associated secretory phenotypes reveal cell-nonautonomous functions of oncogenic RAS and the p53 tumor suppressor, PLoS Biol. 6 (2008) e301.
[59] J.P. Coppe, P.Y. Desprez, A. Krtolica, J. Campisi, The senescence-associated secretory phenotype: the dark side of tumor suppression, Annu. Rev. Pathol. 5 (2010) 99–118, https://doi.org/10.1146/annurev-pathol-121808-102144.
[60] C. Neidlinger-Wilke, F. Galbusera, H. Pratsinis, E. Mavrogonatou, A. Mietsch, D. Kletsas, H.J. Wilke, Mechanical loading of the intervertebral disc: from the macroscopic to the cellular level, Eur. Spine J. 23 (2014) S333–S343, https://doi.org/10.1007/s00586-013-2855-9.
[61] G.T. Desmoulin, V. Pradhan, T.E. Milner, Mechanical aspects of intervertebral disc injury and implications on biomechanics, Spine 45 (2020) E457–E464, https://doi.org/10.1097/brs.0000000000003291.
[62] H. Cherif, M. Mannarino, A.S. Pacis, J. Ragoussis, O. Rabau, J.A. Ouellet, L. Haglund, Single-cell RNA-seq analysis of cells from degenerating and non-degenerating intervertebral discs from the same individual reveals new biomarkers for intervertebral disc degeneration, Int. J. Mol. Sci. 23 (2022), https://doi.org/10.3390/ijms23073993.
[63] M.V. Risbud, E. Schipani, I.M. Shapiro, Hypoxic regulation of nucleus pulposus cell survival *from Niche to notch*, Am. J. Pathol. 176 (2010) 1577–1583, https://doi.org/10.2353/ajpath.2010.090734.
[64] D. Sakai, S. Grad, Advancing the cellular and molecular therapy for intervertebral disc disease, Adv. Drug Deliv. Rev. 84 (2015) 159–171, https://doi.org/10.1016/j.addr.2014.06.009.
[65] C.L. Le Maitre, A.J. Freemont, J.A. Hoyland, Accelerated cellular senescence in degenerate intervertebral discs: a possible role in the pathogenesis of intervertebral disc degeneration, Arthritis Res. Ther. 9 (2007) R45, https://doi.org/10.1186/ar2198.
[66] E.J. Novais, B.O. Diekman, I.M. Shapiro, M.V. Risbud, p16(Ink4a) deletion in cells of the intervertebral disc affects their matrix homeostasis and senescence associated secretory phenotype without altering onset of senescence, Matrix Biol. 82 (2019) 54–70, https://doi.org/10.1016/j.matbio.2019.02.004.
[67] E.J. Novais, V.A. Tran, S.N. Johnston, K.R. Darris, A.J. Roupas, G.A. Sessions, I. M. Shapiro, B.O. Diekman, M.V. Risbud, Long-term treatment with senolytic drugs Dasatinib and Quercetin ameliorates age-dependent intervertebral disc degeneration in mice, Nat. Commun. 12 (2021) 5213, https://doi.org/10.1038/s41467-021-25453-2.
[68] H. Che, J. Li, Y. Li, C. Ma, H. Liu, J. Qin, J. Dong, Z. Zhang, C.J. Xian, D. Miao, et al., p16 deficiency attenuates intervertebral disc degeneration by adjusting oxidative stress and nucleus pulposus cell cycle, Elife (2020) 9, https://doi.org/10.7554/eLife.52570.
[69] M. Saberi, X. Zhang, A. Mobasheri, Targeting mitochondrial dysfunction with small molecules in intervertebral disc aging and degeneration, Geroscience 43 (2021) 517–537, https://doi.org/10.1007/s11357-021-00341-1.
[70] W. Hong, F. Mo, Z. Zhang, M. Huang, X. Wei, Nicotinamide mononucleotide: a promising molecule for therapy of diverse diseases by targeting NAD+ metabolism, Front. Cell Dev. Biol. 8 (2020) 246, https://doi.org/10.3389/fcell.2020.00246.
[71] Y. Song, S. Li, W. Geng, R. Luo, W. Liu, J. Tu, K. Wang, L. Kang, H. Yin, X. Wu, et al., Sirtuin 3-dependent mitochondrial redox homeostasis protects against AGEs-induced intervertebral disc degeneration, Redox Biol. 19 (2018) 339–353, https://doi.org/10.1016/j.redox.2018.09.006.
[72] M. Alini, S.M. Eisenstein, K. Ito, C. Little, A.A. Kettler, K. Masuda, J. Melrose, J. Ralphs, I. Stokes, H.J. Wilke, Are animal models useful for studying human disc disorders/degeneration? Eur. Spine J. 17 (2008) 2–19, https://doi.org/10.1007/s00586-007-0414-y.
[73] Z.-Y. Lu, P.-B. Chen, Q.-Y. Xu, B. Li, S.-D. Jiang, L.-S. Jiang, X.-F. Zheng, Constitutive and conditional gene knockout mice for the study of intervertebral disc degeneration: current status, decision considerations, and future possibilities, JOR SPINE 6 (2023) e1242, https://doi.org/10.1002/jsp2.1242.
[74] G.D. O'Connell, E.J. Vresilovic, D.M. Elliott, Comparison of animals used in disc research to human lumbar disc geometry, Spine 32 (2007) 328–333, https://doi.org/10.1097/01.brs.0000253961.40910.c1.